https://doi.org/10.5194/egusphere-2026-1757
Preprint. Discussion started: 10 April 2026

Sensitivity analysis and scaling of tsunamis generated by granular flows at Stromboli volcano: A numerical modeling approach

Matteo Trolese[1], Matteo Cerminara[1], Tomaso Esposti Ongaro[1], Mattia de'Michieli Vitturi[1], and Alessandro Tadini[1]

[1]Istituto Nazionale di Geofisica e Vulcanologia, Sezione di Pisa, Via C. Battisti 53, Pisa 56125, Italy

Correspondence: Matteo Trolese (matteo.trolese@ingv.it) and Matteo Cerminara (matteo.cerminara@ingv.it)

Abstract. Tsunamis generated by gravitational flows at volcanic islands pose a significant hazard, yet the sensitivity of wave heights to key source parameters remains poorly constrained. Using the non-hydrostatic multilayer HySEA model, we perform an extensive parametric study to assess the sensitivity of granular flow-generated tsunami wave heights at Stromboli volcano to six physical parameters: slide volume, initial submergence depth (elevation), density, basal friction, water-coupling coefficient, and source azimuth. A variance-based Sobol sensitivity analysis reveals that for the combined dataset of subaerial and submarine flows, the initial elevation (contributing $\sim$61% to output variance normalized to 100%) and volume ($\sim$22%) are the dominant controls on maximum wave height. When analyzed separately, subaerial tsunamis are primarily controlled by volume ($\sim$60%), while submarine tsunamis show a balanced sensitivity to volume ($\sim$35%) and initial submergence depth ($\sim$37%). We identify distinct scaling relationships between maximum wave height and landslide volume: a linear one for submarine landslides, with an exponential decay in efficiency as a function of submergence depth; a logarithmic fit for subaerial landslides, where the efficiency of wave generation per unit volume decreases for larger events. These relationships, modulated by secondary parameters like friction, provide a quantitative framework for rapid tsunami hazard assessment. Our results demonstrate a crossover in hazard potential, where subaerial slides tend to produce larger tsunami waves for smaller volumes, while submarine slides can produce larger waves for larger volumes due to the absence of logarithmic saturation. These results constrain the scaling laws needed to quickly invert tsunami observations into source volumes (and viceversa) and improve probabilistic hazard assessments by identifying the parameters that dominate uncertainty at Stromboli and similar islands

1 Introduction

Tsunamis are a type of secondary hazard that can be more devastating than the initial triggering event. They can be generated by earthquakes, landslides, volcanic eruptions, or even asteroid impacts (Paris, 2015; Løvholt et al., 2015; Wünnemann and Weiss, 2015). Tsunamis resulting from volcanic activity, such as volcanic flows or debris avalanches produced by volcano flank instabilities, are under-studied relative to their earthquake-generated counterparts (Løvholt et al., 2020). However, even small volcano-triggered tsunamis can produce significant wave heights along the nearby coasts (Tinti et al., 2006; Auker et al., 2013; Paris et al., 2014; Ioki et al., 2019; Heidarzadeh et al., 2020). A recent example is the 2018 Anak Krakatau event, where a relatively small-scale volcanic collapse triggered a devastating tsunami in the Sunda Strait (Grilli et al., 2019). This is particularly true for volcanic islands, where steep slopes and persistent volcanic activity increase the likelihood of secondary hazards. Indeed, volcanic islands are often subject to voluminous flank failures, crater collapses, and column collapses during paroxysmal events, which can generate massive debris avalanches or pyroclastic density currents (Clare et al., 2023). These phenomena may, in turn, trigger tsunamis capable of propagating over distances of thousands of kilometers from their source (Moore and Moore, 1984; McMurtry et al., 2004; Ramalho et al., 2015; Paris et al., 2017; Rosi et al., 2019). The 1888 event at Ritter Island in New Guinea represents the most significant historical lateral collapse of an island volcano as the failure of ~ 5 km^3 of material triggered a tsunami with 10–15 m amplitudes recorded even at distances of hundreds of kilometers from the source (Ward and Day, 2003).

Volcano-related tsunamis have gained increasing attention in recent years, particularly following high-impact events like the 2018 Anak Krakatau and the 2022 Hunga Tonga-Hunga eruptions (Grilli et al., 2019; Heidarzadeh et al., 2020; Ye et al., 2020; Omira et al., 2022; Kubota et al., 2022). These events represent just a handful of the fatal disasters connected with volcano tsunamis worldwide, with numerous volcanic tsunamis recorded globally since the instrumental era (Schindelé et al., 2024). Understanding the source mechanisms of these tsunamis is therefore important for accurately simulating their initiation, propagation, and coastal amplification, which is key for predicting and mitigating their impacts (Paris et al., 2014; Paris, 2015).

Stromboli, whose activity has been nearly continuous since approximately the VIII century CE, is characterized by persistent Strombolian eruptions that may be punctuated by more intense effusive and explosive phenomena (Barberi et al., 1993; Rosi et al., 2000, 2013; Bevilacqua et al., 2020). Tsunamis at Stromboli have mostly been linked to both subaerial and submarine landslides caused by gravitational instabilities of the Sciara del Fuoco (SdF) – a large scar on the northwestern flank of the volcano representing the preferential runaway of volcanic products – following explosive and/or effusive eruptions (Tinti et al., 2006, 2008; Pistolesi et al., 2020). Large-scale tsunamis resulting from landslides at Stromboli have been documented since the XIV century (Rosi et al., 2019; Pistolesi et al., 2020). In the last century, at least four major tsunamis (characterized by hundreds of meters of water ingression in Stromboli village) and several minor events triggered by landslides along the SdF have affected the shoreline of the Stromboli village (Barberi et al., 1993; Bevilacqua et al., 2020; Pistolesi et al., 2020; Tadini et al., in preparation). Tinti et al. (2006) reported that the last, large tsunami occurred in 2002 was triggered by two landslides with a combined submarine-subaerial volume of $20\text{-}30 \times 10^6\,\mathrm{m}^3$ and had a maximum runup of 11 m along the shoreline. A new modeling of the 2002 event was conducted by Fornaciai et al. (2019) reporting that a submarine landslide would need to have been about three times more voluminous than a subaerial one to cause the observed tsunami damage. Esposti Ongaro et al. (2021) also used this event as a reference to assess the relative sensitivity of numerical predictions to the landslide and the wave models. They concluded that non-hydrostatic, multilayer depth-averaged models are well-suited to reproduce proximal waveforms of landslide-generated tsunamis on volcanic islands. In 2019, a series of pyroclastic flows triggered by two violent explosive eruptions generated tsunamis of 1 – 2 m in height in front of the SdF, although they reached only a few centimeters in maximum elevation along the shoreline (Giordano and De Astis, 2020; Ripepe and Lacanna, 2024). Thanks to new elastic

https://doi.org/10.5194/egusphere-2026-1757
Preprint. Discussion started: 10 April 2026

beacons installed in front of the SdF in the years 2008 and 2017 (Ripepe and Lacanna, 2024), several small tsunamis of about 0.02-2.5 m were recorded in front of the SdF in 2019-2024 (Calvari et al., 2022; Ripepe and Lacanna, 2024). These recurrent events make Stromboli the principal locations in the Southern Tyrrhenian Sea where tsunami induced by volcanic activity are generated.

Modeling landslide-generated tsunamis requires capturing complex source dynamics, such as landslide triggering, propagation, and deformation (Harbitz et al., 2006; Løvholt et al., 2015; Pudasaini and Mergili, 2019), and wave processes, where conventional assumptions fail near steep topographies. This necessitates non-hydrostatic, dispersive formulations (Yavari-Ramshe and Ataie-Ashtiani, 2016). Depth-averaged shallow-water models provide a practical framework widely applied across geophysics, from snow avalanches (Vicari and Issler, 2025) to volcanic flows (Kelfoun et al., 2009, 2017; Shimizu et al., 2017; de' Michieli Vitturi et al., 2019, 2023). For accurate wave propagation, advanced Boussinesq-type formulations resolving dispersion effects have been developed (Kirby et al., 2022). The non-hydrostatic Multilayer HySEA model (Macías et al., 2021a) implements such an approach, efficiently capturing critical bathymetric interactions through adaptive vertical layering. To initialize such a model, several input source parameters are required, including the source location, the volume, density, and shape of the released mass, its rheological parameters, and the strength of its coupling with water. However, these input conditions carry considerable uncertainties due to limited information about the source mechanisms and the complex multiphase dynamics of gravitational flows and their interaction with water. Additionally, estimating these parameters from historical and field analysis remains challenging, as tsunami deposits generated by gravitational flows are often poorly preserved in the geological record or difficult to interpret (Ramalho et al., 2015; Rosi et al., 2019; Dawson et al., 2020). To quantify these uncertainties, multiple simulations can be performed to explore the input parameter space. The number of simulation runs and their resolution have been selected to balance computational cost and model accuracy (Løvholt et al., 2005; Grilli et al., 2017; Fornaciai et al., 2019; Esposti Ongaro et al., 2021; Poulain et al., 2022; Esposti Ongaro et al., 2025).

Our principal aim here is to assess the sensitivity of maximum wave heights at relevant locations to the parameters characterizing the tsunamigenic gravitational flow. Following the same physical and numerical approach as Esposti Ongaro et al. (2021) and Esposti Ongaro et al. (2025), we performed a series of numerical simulations to test the effects of key parameters, namely the landslide elevation (subaerial and submarine), volume, density, shape, friction angles, and the coupling between the landslide and the water. By doing so, we further expand and complement the database presented in Cerminara et al. (2024) and Esposti Ongaro et al. (2021, 2025), enabling a comparison of how these parameters influence the maximum wave height and defining a hierarchy of their relative importance.

2 Simulated scenarios

For our parametric study, we examined a wide range of initial landslide conditions to assess how various parameters involved in the numerical model affect the waveforms, identifying those with the greatest impact on the maximum wave height H. Table 1 shows all the parameters considered and their respective values. Although most of these initial conditions are not meant to represent a specific event occurred at Stromboli, we incorporated some scenarios compatible with those hypothesized for the

2002 event, as previously done by Esposti Ongaro et al. (2021, 2025). We carried out all the numerical simulations of landslide and sea-surface deformation using a topo-bathymetric computational grid with spatial resolution of 20 m (Favalli et al., 2009; Chiocci and Ridente, 2011; Fornaciai et al., 2019, 2024). As shown by Esposti Ongaro et al. (2021), using a 20 m grid at Stromboli affect the maximum wave amplitude by less than 10% with respect to a 10 m grid. We therefore considered the 20 m grid as a good compromise between computational cost and spatial resolution.

We considered 11 landslide initial elevations (q) along 3 different axes (for a total of 33 positions, see Fig. 1) to cover a range of potential spatial variability along the SdF, including both subaerial and submarine mass movements. The spacing of the positions along the two outer axes was adjusted so that all positions maintain approximately the same topographical quota as their corresponding points on the central axis. Each of these initial positions was characterized by varying density (ρ) and volume (V), selected to provide a representative range of potential values. Previous studies (Løvholt et al., 2005; Grilli et al., 2017; Esposti Ongaro et al., 2025) reported that the initial volume of the landslide plays a crucial role in determining the impact of the resulting tsunami, while density has a second-order effect. In our simulations, the landslide volumes range from $3 \times 10^6\,\mathrm{m}^3$ to $30 \times 10^6\,\mathrm{m}^3$. The upper bound was selected based on the 2002 event, which mobilized a total of about $30 \times 10^6\,\mathrm{m}^3$ across multiple discrete phases, including both subaerial and submarine landslides (Fornaciai et al., 2019). We also explored smaller volumes down to $3 \times 10^6\,\mathrm{m}^3$ to represent events with higher probabilities of occurrence and to assess their relationship with waveforms. The densities considered were 1700, 2000, and 2500 kg/m^3, chosen to reflect reasonable values for gravitational flows composed of solid, liquid, and gas phases. Although the bulk density could change as the granular flow transitions from subaerial to submarine environments, our sensitivity analysis (presented later) confirms its negligible impact relative to volume.

For the rheological properties of the simulated landslides, we adopted the Coulomb-type friction law proposed by Pouliquen and Forterre (2002), which has been widely used for granular flow modeling (Mangeney et al., 2007; Lucas et al., 2014; Brunet et al., 2017). This friction law is characterized by three friction angles (δ_1, δ_2, δ_3, hereafter collectively referred to as δ): δ_1 and δ_2, which are the static and dynamic angles of the material, respectively, and δ_3, which represents the dependence of the friction coefficient on flow thickness and velocity (see Appendix A). According to this law, as the thickness of the granular layer decreases and its velocity increases, the friction increases, and vice versa. In our parametric study, we varied the friction angles in 6 different configurations: $[5, 7.5, 5]^\circ$, $[10, 15, 10]^\circ$, $[15, 22.5, 15]^\circ$, $[20, 30, 20]^\circ$, $[25, 37.5, 25]^\circ$, and $[30, 45, 30]^\circ$. These values were chosen to explore a wide range of potential frictional properties (Pouliquen and Forterre, 2002; Brunet et al., 2017; Poulain et al., 2022; Esposti Ongaro et al., 2025), while maintaining $\delta_1 = \delta_3$ for simplicity, as done in previous studies (Esposti Ongaro et al., 2021, 2025). Since our focus is on gravitational mass movements in general (not limited to landslides, pyroclastic flows, or lahars), the range of variation in certain parameters, such as the friction angles, is intentionally broad to capture the diversity of phenomena under investigation. Additionally, we tested several values of the friction between the landslide and the water layer (m_f), with $m_f \in [10^{-5}, 10^{-4}, 10^{-3}, 10^{-2}, 10^{-1}]\ \mathrm{m}^{-1}$, similar to previous papers (González-Vida et al., 2019; Poulain et al., 2022; Svennevig et al., 2024) (see Appendix A).

For each of the 6 friction angle sets, we combined the 6 volumes, 3 densities, and 11 elevations along the central source azimuth ($D = 320.2^\circ$, transect B in Fig. 1) with a fixed $m_f = 10^{-3}\ \mathrm{m}^{-1}$. Similarly, for each of the 5 m_f values, we used the

Table 1. Input parameters space explored with the simulated scenarios

Parameter	**Value**
Slide volume V $\left(\mathrm{m}^3 \times 10^6\right)$	3.0; 5.0; 8.7; 14; 21; 30
Slide density ρ $\left(\mathrm{kg\,m}^{-3}\right)$	1700; 2000; 2500
Slide initial elevation q (m asl)	530; 328; 197; 42; -63; -180; -280; -375; -445; -514; -583
Source azimuth D (deg)	312; 320.2; 327.9
Friction angles $\delta_1, \delta_2, \delta_3$ (deg)	(5, 7.5, 5)°; (10, 15, 10)°; (15, 22.5, 15)°;
	(20, 30, 20)°; (25, 37.5, 25)°; (30, 45, 30)°
Water-slide coupling m_f $\left(\mathrm{m}^{-1}\right)$	10^{-5}; 10^{-4}; 10^{-3}; 10^{-2}; 10^{-1}

friction angle set $[10, 15, 10]°$, maintaining the same combinations of 6 volumes, 3 densities, and 11 elevations. Additionally, for the 11 initial elevations along the lateral northern and southern axes (transect A and C in Fig. 1, respectively), we used the friction angle set $[10, 15, 10]°$ and $m_f = 10^{-3}\ \mathrm{m}^{-1}$, while varying the 6 volumes and 3 densities. The combination of all parameters resulted in a total of $6 \times 11 \times 3 \times (6 + 5 + 3) = 2772$ simulated scenarios, which have been collected in a SQL database.

For each run, we focused our analysis on the waveforms (timeseries of the sea surface elevation) at specific locations. In particular, we sampled waveforms at 11 different locations, corresponding to 1) two tsunami gauges (elastic beacons) deployed aside the SdF slope, positioned 260 m and 350 m from Punta dei Corvi (PDC) and Punta Labronzo (PLB) capes, respectively (Lacanna and Ripepe, 2020), and 2) nine virtual gauges positioned around Stromboli island, representing the villages of Stromboli (gauges 7, 8, and 9) and Ginostra (10). The locations of these sampling points are shown in Figure 1 and their exact coordinates are detailed in Supplementary Material.

3 Methods

3.1 Numerical Model

We performed simulations using the Multilayer-HySEA model (Macías et al., 2021a, b), which simulates the coupled motion of granular flows (submarine or subaerial) and the resulting tsunami. The model accounts for non-linear effects and preserves the correct dispersion relationship, not only in shallow waters but also in intermediate depth regimes (Peregrine, 1972). The model is part of the HySEA high performance software package developed by the EDANYA group at the University of Málaga (Fernández-Nieto et al., 2008), and has been successfully used to simulate tsunamis generated by landslides at the laboratory and field scale (Esposti Ongaro et al., 2021; Macías et al., 2021b; Poulain et al., 2022; Kirby et al., 2022; Poulain et al., 2023). The granular flow is modeled using depth-averaged equations for a thin layer, with the landslide treated as an incompressible, homogeneous granular fluid governed by the Pouliquen and Forterre (2002) friction law. Water flow is simulated with

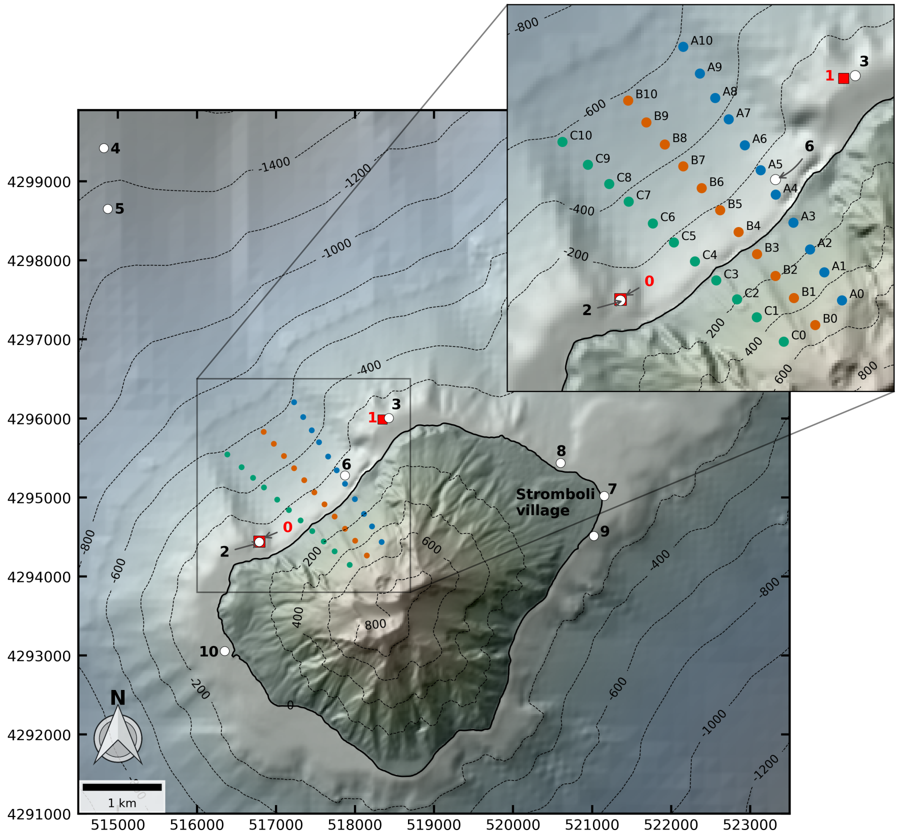

Figure 1. Topography and bathymetry of Stromboli Island, Italy, and its surroundings, used for numerical simulations. Contour lines are shown at intervals of 200 m. White dots indicate the positions of virtual gauges (1, 2, 4, 5, 6, 7, 8, 9, and 10), while red squares represent real gauges (0 and 1). Simulated wave data are sampled at all these gauge locations. The figure also shows the 3 transects corresponding to all landslide initial elevations along the selected source azimuths (Tab. 1), marked in blue, red, and green, which are detailed in the enlargement. Coordinates are expressed in the WGS-84 UTM Zone 33N system

.

a multilayer non-hydrostatic shallow-water system (Fernández-Nieto et al., 2018), allowing for the accurate representation of dispersive wave effects, which are critical for steep bathymetric slopes or when wavelength-to-depth ratios are significant. The model solves the equations using an efficient hybrid finite-volume-finite-difference scheme on GPU-accelerated architectures (Escalante et al., 2019; Macías et al., 2020).

3.2 Sensitivity analysis

We used the Sobol method (Sobol, 2001; Homma and Saltelli, 1996; Gatel et al., 2019), a variance-based global sensitivity analysis, to quantify the contribution of each input parameter to the variance of H through the computation of first-order and total Sobol indices using the `scipy.stats.sobol_indices` implementation provided by the SciPy library (v1.17.0; Virtanen et al., 2020). Because the numerical database is available only for a discrete set of parameter combinations, the model response was first represented by a multidimensional interpolating function using `RegularGridInterpolator`. The Sobol indices were then computed by sampling this interpolated response surface with 2^{15} quasi-random points drawn from uniform distributions spanning the range of each input parameter. The first-order sensitivity index S (Sobol, 1993) represents the fraction of the output variance attributed to a specific variable, without taking into account its interactions with other variables. In contrast, the total sensitivity index S_T (Homma and Saltelli, 1996) represents the fraction of output variance associated with an input parameter, including its interactions of any order with other parameters. Accordingly, the first-order index quantifies the additive contribution of each input parameter, whereas the total index includes both its additive contribution and its participation in non-additive effects with the other parameters. The input parameters considered in the analysis are V, q, ρ, δ, m_f, and D. In a model without interactions between inputs, the sum of the first-order indices ($\sum_k S_k$, k running across input parameters) and the sum of the total indices ($S_T \equiv \sum_k S_{T_k}$) are both equal to 1. However, in models with interactions, $\sum_k S_k < 1$, while $S_T \equiv \sum_k S_{T_k} > 1$. In particular, defining $\Delta_k \equiv S_{T_k} - S_k$ as the difference between the total and first-order indices of the k-th parameter, Δ_k measures how strongly the k-th parameter is involved in non-additive effects. More generally, the quantity $1 - \sum_k S_k$ represents the fraction of output variance explained by all non-additive contributions. Likewise, the quantity $\sum_k S_{T_k} - 1$ also reflects the presence of non-additive effects, although higher-order terms contribute to it with a different weight. In the present application, however, the quantities

$$\frac{1}{2}\sum_k \Delta_k, \qquad 1 - \sum_k S_k, \qquad \sum_k S_{T_k} - 1$$

are found to be nearly identical, indicating that non-additive effects are dominated by pairwise contributions and that higher-order terms are negligible. For an overall synthesis that aims to compare the general sensitivity of one parameter to the others, a normalization procedure of the total indices is useful. While this approach loses detail on how much of the sensitivity to a given parameter is due to non-additive effects, it provides a more intuitive measure of the sensitivity of each parameter within a space that sums to 100%. For completeness, the full set of Sobol indices, including non-additive terms, is provided in Supplementary Material. There, all indices are calculated for each gauge and for each dataset (listed below), and their average across all gauges is also reported. Given the scenarios presented, a complete sensitivity analysis can be performed on the following datasets:

1. Reference dataset, denoted as $(\cdot)^r$, consisting of $6 \times 11 \times 3 = 198$ scenarios for the (V, q, ρ) set of parameters;
2. Extended dataset with landslide friction angles, denoted as $(\cdot)^\delta$, consisting of $6 \times 11 \times 3 \times 6 = 1188$ scenarios for the (V, q, ρ, δ) set of parameters;
3. Extended dataset with landslide-water coupling, denoted as $(\cdot)^{m_f}$, consisting of $6 \times 11 \times 3 \times 5 = 990$ scenarios for the (V, q, ρ, m_f) set of parameters;
4. Extended dataset with transect direction, denoted as $(\cdot)^D$, consisting of $6 \times 11 \times 3 \times 3 = 594$ scenarios for the (V, q, ρ, D) set of parameters.

https://doi.org/10.5194/egusphere-2026-1757
Preprint. Discussion started: 10 April 2026

In theory, a larger dataset with $6 \times 11 \times 3 \times 6 \times 5 \times 3 = 17820$ scenarios should be considered to perform a complete Sobol analysis, capturing the variability across all six parameters $(V, q, \rho, \delta, m_f, D)$. However, the dataset analyzed in this study lacks the 6-dimensional parameter hypercube sections that represent interactions among the three secondary parameters (δ, m_f, D). An estimate of the Sobol parameters can still be obtained using the available 2772 scenarios without fully exploring the hypercube. One approach to assess the feasibility of this approximation is to check whether the normalized Sobol indices for the primary parameters V, q, ρ obtained from the reference dataset (Supplementary Material, Tables S2–S4) are similar to those obtained from the three datasets extended with one secondary parameter (Supplementary Material, Tables S5–S13). To this aim, we define the following normalization procedure:

$$s_k = S_{T_k}/S_T\,, \quad \text{with } k \in [V, q, \rho, \delta, m_f, D],$$

so that:

$$s_V^r + s_q^r + s_\rho^r = 1,$$

in the reference dataset, and:

$$s_V^j + s_q^j + s_\rho^j = 1 - s_j^j\,, \quad \text{with } j \in [\delta, m_f, D],$$

in the three datasets extended with one secondary parameter ($j \in [\delta, m_f, D]$). In this latter case, a second normalization is needed to ensure that the Sobol indices corresponding to the three primary parameters sum to one. Namely:

$$z_i^j = \frac{s_i^j}{1 - s_j^j}\,, \quad \text{with } i \in [V, q, \rho] \text{ and } j \in [\delta, m_f, D],$$

so that:

$$z_V^j + z_q^j + z_\rho^j = 1\,, \quad \text{with } j \in [\delta, m_f, D].$$

When the extension of the reference dataset with one of the secondary parameters does not affect significantly the normalized indices, we expect:

$$s_i^r \simeq z_i^\delta \simeq z_i^{m_f} \simeq z_i^D \text{ with } i \in [V, q, \rho],$$

where the Sobol index on the left hand-side comes from the reference dataset, and those on the right hand-side come from the secondary parameter datasets. This comparison is shown in Supplementary Material (Tables S14–S16) for each gauge and the average across all gauges. The variability between the four datasets for each primary parameter is measured by the standard deviation σ_i, with $i \in [V, q, \rho]$. Overall, the estimate of the normalized total Sobol indices obtained from the reference dataset aligns well with those obtained from the extended datasets, and σ_i remains small. In particular, the average values across all gauges of $(\sigma_V, \sigma_q, \sigma_\rho)$ are $(0.6, 0.6, 0.0)\%$ when subaerial and submarine cases are considered together, $(1.0, 1.0, 0.1)\%$ for subaerial cases, and $(2.6, 2.6, 0.1)\%$ for submarine cases.

We thus show that, for this specific application, the normalized Sobol indices do not change significantly when an additional parameter is included. This result supports the estimation of the sensitivity with respect to all six parameters together, using the information contained in the reduced dataset currently available. To do so, we first define:

$$z_i = \frac{1}{4}\left(s_i^r + \sum_{j\in[\delta,m_f,D]} z_i^j\right) \quad \text{with } i \in [V,q,\rho],$$

as the average across the four datasets for each primary parameter. For the secondary parameters, we instead use $z_j = z_j^j$ with $j \in [\delta, m_f, D]$ to maintain the same normalization as defined for z_i^j. Finally, the normalized Sobol parameters Z_k, with $k \in [V,q,\rho,\delta,m_f,D]$, are obtained by scaling z_k such that $Z_V + Z_q + Z_\rho + Z_\delta + Z_{m_f} + Z_D = 1$. This is a measure of the relative sensitivity to a parameter with respect to the others, neglecting interactions between secondary parameters, but taking into account the interactions among primary parameters and with each of the secondary parameters.

3.3 Volume–wave height fitting functions

To characterize the relationship between V and H, we fitted the simulation data using two functional forms. These were selected to capture both the approximately linear behavior observed in submarine cases and the logarithmic trend apparent in subaerial scenarios (see Sect. 4.3).

The first function assumes a simple linear dependency of H on the landslide volume V:

$$H(V) = \alpha_{\text{lin}} V, \tag{1}$$

where α_{lin} represents the slope (i.e., angular coefficient) of the linear fit and quantifies the wave height generated per unit volume of landslide (in $\frac{\text{m}}{10^6\,\text{m}^3}$).

The second function captures the logarithmic behavior observed in subaerial cases:

$$H(V) = \alpha_{\log} V_{\log} \ln\left(1 + \frac{V}{V_{\log}}\right), \tag{2}$$

The two parameters in Eq. (2) have a clear interpretation. Differentiating with respect to V gives $H'(V) = \frac{\alpha_{\log}}{1+V/V_{\log}}$, so that, in particular, $H'(0) = \alpha_{\log}$. Therefore, for $V \ll V_{\log}$, Eq. (2) reduces to $H(V) \approx \alpha_{\log} V$, and $\alpha_{\log}$ can be interpreted as the expected increase in H per unit landslide volume in the small-volume regime, with the same units as α_{lin}. The parameter $V_{\log}$, which has units of volume, represents the characteristic crossover scale between the initial linear regime and the logarithmic regime. Indeed,

$$\frac{\alpha_{\log}}{H'(V)} = 1 + \frac{V}{V_{\log}}, \tag{3}$$

which shows that the local slope decreases to $\alpha_{\log}/2$ at $V = V_{\log}$. More generally, $V_{\log}$ quantifies the range over which the approximation $H'(V) \approx \alpha_{\log}$ remains valid: for example, at $V = \frac{1}{10} V_{\log}$ one has $H'(V) = 0.91\,\alpha_{\log}$, whereas at $V = \frac{1}{2} V_{\log}$ one has $H'(V) = 0.67\,\alpha_{\log}$. Summarizing, to ensure physical consistency and to preserve a direct interpretation of the model parameters, the function is defined such that:

- $H(0) = 0$, i.e., in the absence of a landslide no wave is generated;
- $H'(0) = \alpha_{\text{log}}$, so that α_{log} represents the proportionality coefficient in the small-volume limit;
- $H'(V_{\text{ref}}) = \alpha_{\text{ref}}$, where α_{ref} denotes the local coefficient at a prescribed reference volume V_{ref} and accounts for the reduction of the slope with increasing volume. With this definition, the characteristic transition scale can be written as

$$V_{\text{log}} = \frac{\alpha_{\text{ref}}}{\alpha_{\text{log}} - \alpha_{\text{ref}}} V_{\text{ref}}.$$

In the following, the reference volume is fixed at $V_{\text{ref}} = 30 \cdot 10^6\,\text{m}^3$. In the limiting case $\alpha_{\text{ref}} \to \alpha_{\text{log}}$, which for fixed V_{ref} is equivalent to $V_{\text{log}} \to \infty$, Eq. (2) tends to Eq. (1), with $\alpha_{\text{log}} = \alpha_{\text{lin}}$. More generally, when $V \ll V_{\text{log}}$, the logarithmic model behaves approximately linearly. This formulation therefore provides a smooth transition from an initially linear trend at small volumes to a more gradual increase at larger volumes, consistent with the expected behavior of subaerial flows, which undergo spreading and energy dissipation before impacting the water. The fitting was performed separately for each gauge location and scenario subset, allowing a detailed comparison among locations and across parameter configurations.

3.4 Source elevation–wave height fitting functions

As we will show and discuss in our sensitivity analysis (Sect. 4), whereas in subaerial cases the volume–wave height coefficient α is effectively independent of source elevation, for submarine sources the coefficient decays systematically with increasing depth. We model this behavior with an exponential decay:

$$\alpha(s) = \alpha_0 \, e^{-s/s_0}\,, \tag{4}$$

where: s is the submergence depth (positive downward), defined as $s = -q$ if q is the source elevation relative to mean sea level; α_0 is the slope at zero submergence (i.e. at the shoreline or just below the waterline); s_0 is the e-folding depth, i.e. the characteristic depth over which α decreases by a factor of e. Equation (4) captures the progressively reduced transfer of landslide momentum to the free surface with depth, due to increased water loading and geometric dispersion. Fitting function parameter values and uncertainty obtained for each gauge are reported in Sect. 4 and in Table 3.

4 Results

4.1 Waveforms

Figure 2 shows an example of the waveforms recorded at gauges in front of the SdF (gauges 0 and 1), offshore (gauge 4), and near Stromboli village (gauge 8). These waveforms are associated with subaerial granular flows of $3 \times 10^6\,\text{m}^3$ and $30 \times 10^6\,\text{m}^3$, both originating from the same initial elevation (B0, see Fig. 1). Each landslide is characterized by a constant density and varying friction angles. The H increases from ∼4 m to ∼22 m in front of the SdF (gauge 1) as the landslide volume increases from $3 \times 10^6\,\text{m}^3$ to $30 \times 10^6\,\text{m}^3$. A similar correlation is observed at more distal locations (gauges 4 and 8). It is interesting

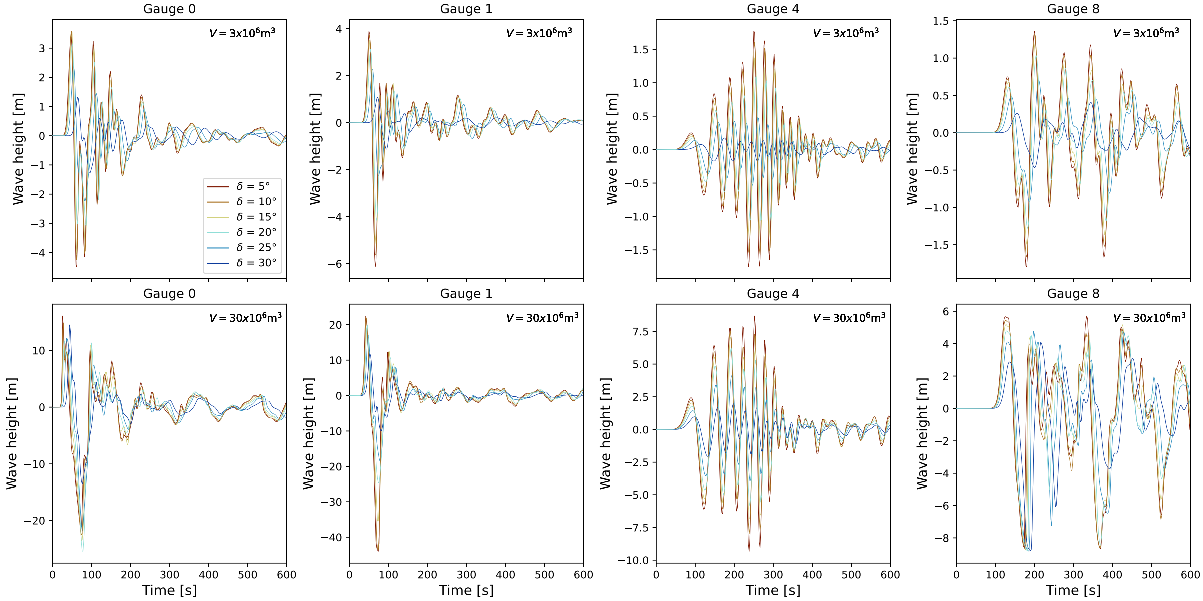

Figure 2. Waveforms recorded at gauges located in front of the SdF (Gauges 0 and 1), offshore (Gauge 4), and near Stromboli village (Gauge 8) for subaerial landslides of $3 \times 10^6\,\mathrm{m}^3$ (top panels) and $30 \times 10^6\,\mathrm{m}^3$ (bottom panels). The waveforms correspond to six configurations of friction angles $\delta_1 = \delta_3 = \{5, 10, 15, 20, 25, 30\}^\circ$, shown in different colors. The landslide-water coupling m_f is fixed at $10^{-3}\ \mathrm{m}^{-1}$, and the density is fixed at $1700\ \mathrm{kg/m}^3$. Both landslides originate from the same subaerial initial elevation (B0, see Fig. 1)

to note that offshore, waveforms appear as a wave packet, exhibiting dispersive wave trains with increasing amplitude before gradually dissipating, whereas those near the SdF are more heterogeneous (Fig. 2). This is because offshore, the different phase and group velocities tend to spread out the wave.

Figure 3 shows waveforms recorded at the same gauges but for submarine flows originating from position B7 (see Fig. 1). Similar to the subaerial case, wave amplitude increases with landslide volume, although the maximum wave heights for submarine landslides are generally smaller. For example, at gauge 0, the wave height for a submarine landslide with a volume of $30 \times 10^6\,\mathrm{m}^3$ reaches ∼2 m, compared to ∼22 m observed in the subaerial case (Fig. 2).

To investigate the information content of the waveforms and how they alter in response to different landslides, different signal metrics can be applied. These include the peak amplitude (i.e., H) and the integral of the waveforms over time, providing insights into the intensity and temporal evolution of the signal. We conducted the analysis using both approaches and found that the overall results were essentially the same, with both waveform characterizations leading to similar conclusions. We present the following analysis in this paper based on H, while the results using the integrated waveform are provided in the Supplementary Material.

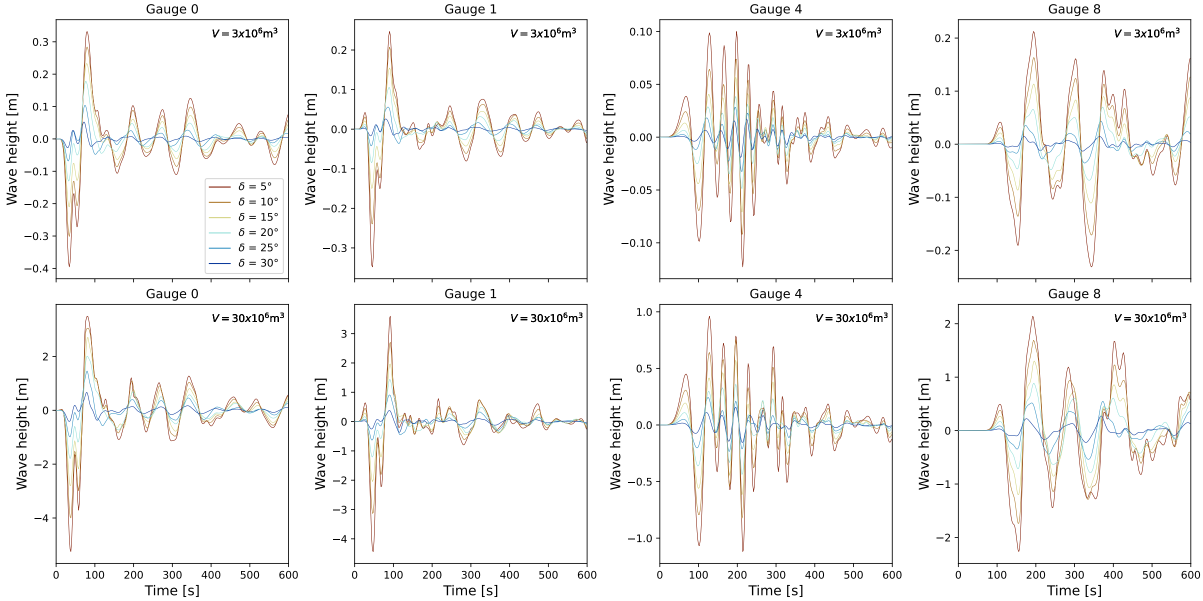

Figure 3. Waveforms recorded at gauges located in front of the SdF (Gauges 0 and 1), offshore (Gauge 4), and near Stromboli village (Gauge 8) for submarine landslides of 3×10^6 m^3 (top panels) and 30×10^6 m^3 (bottom panels). The waveforms correspond to six configurations of friction angles $\delta_1 = \delta_3 = \{5, 10, 15, 20, 25, 30\}^\circ$, shown in different colors. The landslide-water friction coefficient m_f is fixed at 10^{-3} m^{-1}, and the density is fixed at 1700 kg/m^3. Both landslides originate from the same submarine initial elevation (B7, see Fig. 1)

4.2 Sensitivity

The normalized total indices for each gauge and the average across all gauges are shown in Fig. 4. The first section refers to the combined subaerial-submarine case, while the second and third sections refer to the subaerial and submarine cases, respectively. For the combined dataset, V and q are found to be the most influential parameters with average normalized Sobol indices of 21.7% and 61.1%, respectively. The third primary parameter, ρ, has a negligible contribution (0.1%), while the secondary parameters δ, m_f, and D contribute, on average, 11.5%, 2.9%, and 2.7%, respectively. The normalized total indices therefore indicate that, when subaerial and submarine scenarios are analyzed together, the relative sensitivity of H is dominated by source elevation q, followed by landslide volume V. The parameter δ exhibits substantial variability across the gauges, ranging from 3.6% at gauge 0 to 22.7% at gauge 5, indicating that its relative importance is strongly location dependent. Gauge 0 shows a peculiar dependence on source azimuth, probably due to its proximity to the source.

Results for subaerial cases indicate that V is the utmost influential parameter controlling H, with an average contribution of 59.5%, while q accounts for only 3.0%. The secondary parameters δ, m_f, and D collectively explain a larger fraction of the variance, with δ contributing the most (21.6% on average). Similar to the combined dataset, ρ remains negligible. Results for subaerial cases indicate that V is the dominant parameter controlling H, with an average normalized total index of 59.5%, whereas q accounts for only 3.0%. The secondary parameters δ, m_f, and D jointly account for a substantial part of the

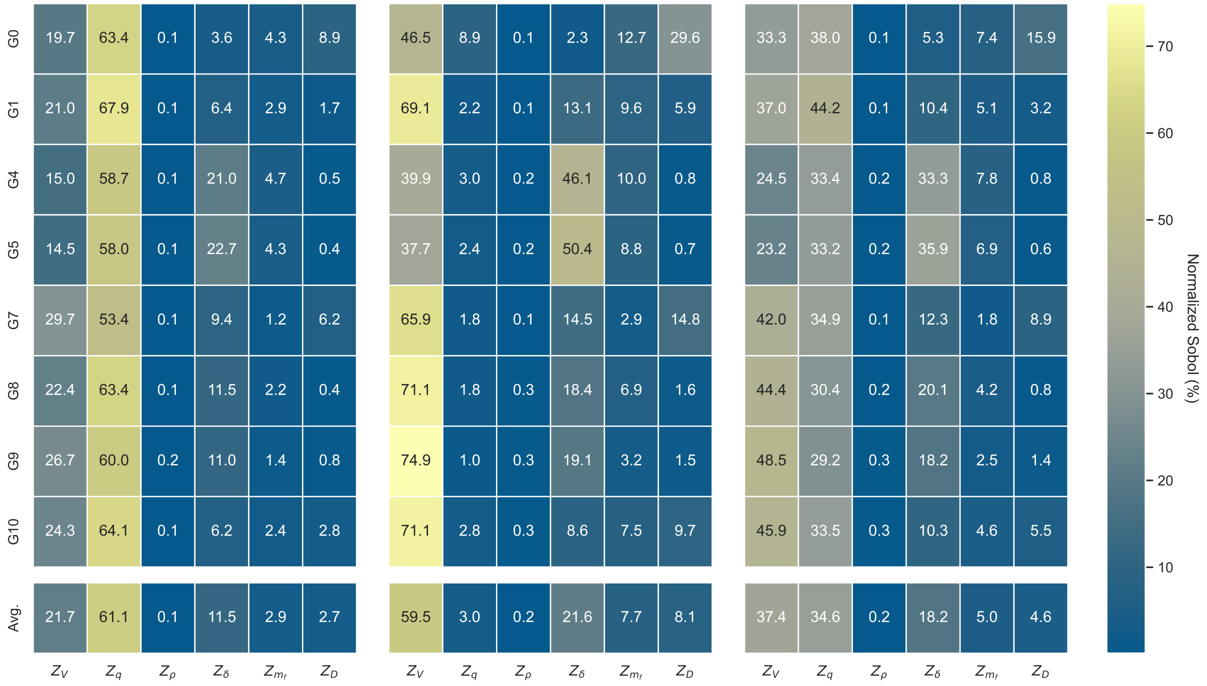

	Z_V	Z_q	Z_ρ	Z_δ	Z_{m_f}	Z_D	Z_V	Z_q	Z_ρ	Z_δ	Z_{m_f}	Z_D	Z_V	Z_q	Z_ρ	Z_δ	Z_{m_f}	Z_D
G0	19.7	63.4	0.1	3.6	4.3	8.9	46.5	8.9	0.1	2.3	12.7	29.6	33.3	38.0	0.1	5.3	7.4	15.9
G1	21.0	67.9	0.1	6.4	2.9	1.7	69.1	2.2	0.1	13.1	9.6	5.9	37.0	44.2	0.1	10.4	5.1	3.2
G4	15.0	58.7	0.1	21.0	4.7	0.5	39.9	3.0	0.2	46.1	10.0	0.8	24.5	33.4	0.2	33.3	7.8	0.8
G5	14.5	58.0	0.1	22.7	4.3	0.4	37.7	2.4	0.2	50.4	8.8	0.7	23.2	33.2	0.2	35.9	6.9	0.6
G7	29.7	53.4	0.1	9.4	1.2	6.2	65.9	1.8	0.1	14.5	2.9	14.8	42.0	34.9	0.1	12.3	1.8	8.9
G8	22.4	63.4	0.1	11.5	2.2	0.4	71.1	1.8	0.3	18.4	6.9	1.6	44.4	30.4	0.2	20.1	4.2	0.8
G9	26.7	60.0	0.2	11.0	1.4	0.8	74.9	1.0	0.3	19.1	3.2	1.5	48.5	29.2	0.3	18.2	2.5	1.4
G10	24.3	64.1	0.1	6.2	2.4	2.8	71.1	2.8	0.3	8.6	7.5	9.7	45.9	33.5	0.3	10.3	4.6	5.5
Avg.	21.7	61.1	0.1	11.5	2.9	2.7	59.5	3.0	0.2	21.6	7.7	8.1	37.4	34.6	0.2	18.2	5.0	4.6

Figure 4. Normalized Sobol indices (Z, Section 3.2) calculated for each parameter and associated with each gauge for the combined subaerial-submarine case (left panel), the subaerial case (middle panel), and the submarine case (right panel). The last row reports the averaged value for each parameter across all gauges

normalized total sensitivity, with δ contributing the most (21.6% on average). Similar to the combined dataset, ρ remains 300 negligible. The distribution of sensitivity values across gauges for the secondary parameters highlights localized variations in their relative importance. For example, gauge 4 shows a pronounced sensitivity to δ (46.1%), significantly exceeding the average, indicating the importance of this parameter offshore of the SdF.

Results for submarine cases demonstrate that q and V have a balanced relative importance, with average normalized total indices of 37.4% and 34.6%, respectively. Compared to the other cases, the secondary parameters δ, m_f, and D have relatively 305 lower contributions, with average values of 18.2%, 5.0%, and 4.6%, respectively. However, the variability of these values across gauges is less pronounced, suggesting more uniform sensitivity distributions in submarine scenarios, even if δ is still important offshore of the SdF.

It should be noted that the normalized total Sobol indices shown in Fig. 4 are useful to rank the relative importance of the parameters, but they do not explicitly show how much of the sensitivity is associated with their interactions. For this reason, 310 the complete set of non-normalized first-order and total Sobol indices is reported in Supplementary Material for each dataset, for each gauge, and for the average across all gauges. To summarize the role of non-additive effects, Table 2 reports the quantity $\Delta_k = S_{T_k} - S_k$, averaged across all gauges, which measures how strongly each parameter is involved in non-additive effects. When all scenarios are analyzed together, Δ_k is generally of the order of 10–15%, indicating appreciable non-additive contributions. In this case, the largest values are associated with q, and, in the extended (δ) dataset, also with δ, showing that source elevation is the parameter most consistently involved in interaction effects. In contrast, for the subaerial subset, Δ_k decreases to only a few percent, indicating a response that is much closer to additive. Here, the largest gaps are associated with V and with the secondary parameters included in the analysis, whereas q plays only a minor non-additive role. For the submarine subset, interaction levels increase again to about 6–10%, with the largest Δ_k values once more associated with q and, when included, with δ. Overall, these results indicate that non-additive effects are weak in subaerial scenarios, but become appreciable when submarine sources are considered, where the effect of source elevation is more strongly entangled with the other controls on wave generation.

Table 2. Comparative table of mean Δ_k values grouped by scenario

Scenarios	Dataset	Δ_V	Δ_q	Δ_ρ	Δ_δ	Δ_{m_f}	Δ_D
all	Reference	10.1	10.1	0.1	-	-	-
	Extended (δ)	11.1	14.5	0.1	6.7	-	-
	Extended (m_f)	10.0	11.8	0.2	-	2.8	-
	Extended (D)	10.3	11.6	0.1	-	-	2.5
subaerial	Reference	1.0	1.0	0.1	-	-	-
	Extended (δ)	4.0	2.4	0.1	4.7	-	-
	Extended (m_f)	3.3	1.4	0.3	-	3.3	-
	Extended (D)	3.3	1.0	0.1	-	-	3.2
submarine	Reference	6.2	6.2	0.1	-	-	-
	Extended (δ)	8.6	9.5	0.1	6.4	-	-
	Extended (m_f)	6.5	7.8	0.3	-	3.6	-
	Extended (D)	6.9	7.6	0.1	-	-	3.4

4.3 Variability of the maximum wave height

Figure 5 shows the variability in H as a function of the landslide volume for a specific submarine elevation (B7 in Fig. 1). Each data point in the scatter plot represents a combination of friction angle and landslide density (with each friction angle corresponding to three symbols due to varying densities). For all these simulations, m_f is fixed at 10^{-3} m^{-1}. Overall, an increasing spreading in maximum sea surface elevation is observed as the volume increases due to different friction angles. In particular, the figure reveals a systematic dependence of the maximum wave height on δ as, for any given volume, lower friction angles consistently produce higher maximum wave heights across all gauges. As it would be expected, the lowest friction angles correspond to weaker basal resistance, which allows for a higher velocity and acceleration of the granular mass, leading to a more efficient energy transfer to the water column. On the other hand, the variability due to density is less significant, as shown by the close grouping of the different symbols for each friction angle. Coherently with the sensitivity results, this indicates that δ has a stronger influence on H, potentially introducing uncertainty into wave height predictions for larger events.

Figure 5 also shows a generally linear correlation between V and H for submarine landslides, modulated by the friction angle. This linearity allows us to make estimates, with a certain margin of error, as the slope of the fit ($\alpha_{\text{log}} \simeq \alpha_{\text{ref}} \simeq \alpha_{\text{lin}}$) indicates how many meters of wave height are expected per million cubic meters of landslide. For example, we expect to record a maximum wave height of $\alpha_{\text{lin}} \simeq 8$ cm per $10^6\,\text{m}^3$ of landslide in front of the SdF (gauge 0), while around the Stromboli village, it ranges from 3 to 9 cm per $10^6\,\text{m}^3$ (gauges 7, 8, and 9).

To quantify the uncertainty in wave amplitude, we introduce two metrics: σ_χ, which measures the root-mean-square relative deviation of the data from the fitted model, capturing how much the observed amplitudes deviate from the predicted values, and σ_α, which estimates the parameter uncertainty in the coefficient α, reflecting the spread in model predictions due to variability in granular mass dynamics (i.e., $\rho, \delta, m_f,$ and D). These metrics are defined as:

$$\sigma_\chi = \sqrt{\frac{1}{N}\sum_{i=1}^{N}\left(\frac{H_i}{H(V_i)} - 1\right)^2},$$

$$\sigma_\alpha = \left(\frac{\alpha_{\text{max}} - \alpha_{\text{min}}}{\alpha_{\text{max}} + \alpha_{\text{min}}}\right),$$

where N is the number of data points, H_i and $H(V_i)$ are the observed and modeled (Eq.s 1 and 2) wave amplitudes, respectively, and α_{max} and α_{min} represent the coefficients (α_{log}) obtained by fitting the model to the maximum and minimum observed wave amplitudes for each volume, respectively.

For the submarine dataset with variable δ (Fig. 5), σ_χ ranges from 43.2% (gauge 0) to 64.9% (gauge 7), while σ_α exceeds 80% at most locations, reaching 94.1% at gauge 7. This highlights that the influence of V on H is strongly modulated by the variability of δ.

Figure 6 illustrates a similar plot but for subaerial granular flows originating from position B0 (see Fig. 1). In contrast to the submarine case, subaerial flow data show a nonlinear relationship marked by a logarithmic trend. While a general dependence on δ is still visible, the relationship is less systematic than in the submarine scenarios, with some gauges showing an overlap or a more scattered distribution of the maximum wave heights across different friction angles. In the present case, for $V < 10 \times 10^6\,\text{m}^3$, the slope of the fit suggests a maximum wave height of $\alpha_{\text{log}} \simeq 80$ cm per $10^6\,\text{m}^3$ in front of the SdF (gauge 0), and $\alpha_{\text{log}} \simeq 34$ cm near the Stromboli village (averaging gauges 7, 8, and 9). However, as the landslide volume increases, these values diminish: at $V = V_{\text{ref}} = 30 \times 10^6\text{m}^3$, coefficients decreases to $\alpha_{\text{ref}} \simeq 27$ cm (gauge 0) and $\alpha_{\text{ref}} \simeq 16$ cm around the village, reflecting the logarithmic nature of the relationship between H and V in the subaerial case. It is interesting to note that σ_χ values (27.5 - 50.0%) are lower than in the submarine scenarios, although σ_α remains significant (61.2 - 92.9%) with gauge 4 and 5 showing the highest uncertainty in coefficient estimates.

In Figure 7, the dependence of H on m_f is analyzed for submarine landslides (B7, see Fig. 1) across different volumes. We see that H consistently increases across locations as m_f decreases (from 10^{-1} to 10^{-5} m^{-1}). This inverse relationship occurs because lower m_f reduces resistance between the submerged granular material and the water column, enabling faster

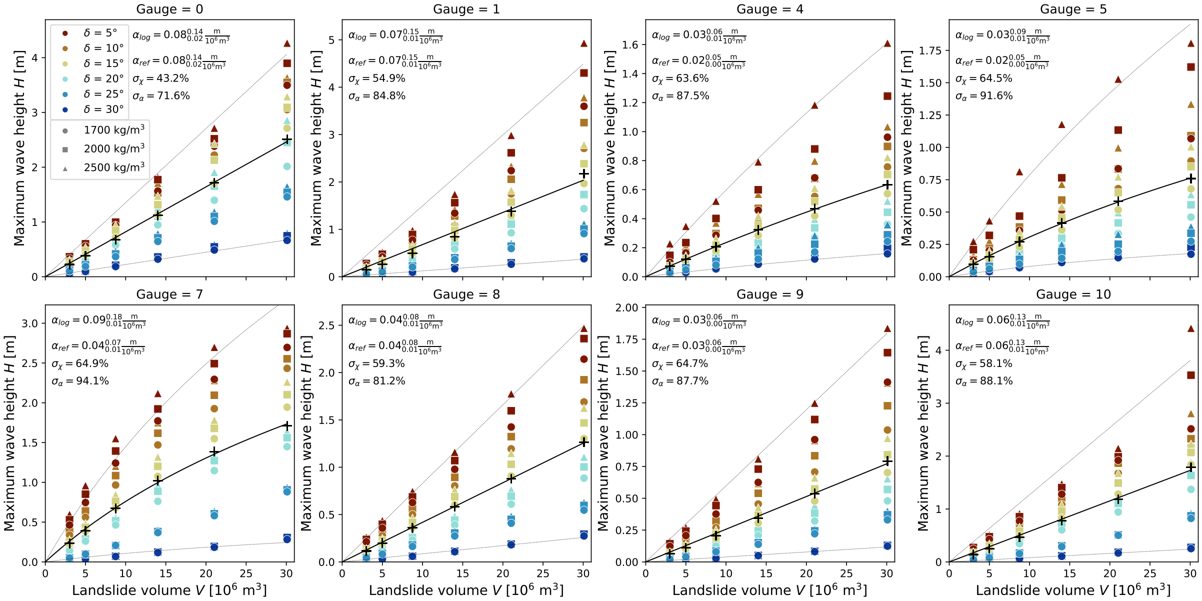

Figure 5. Variability of the maximum wave height as a function of the landslide volume for a fixed submarine elevation (B7, see Fig. 1). The wave height is shown for 6 different configurations of friction angles ($\delta_1 = \delta_3 = \{5, 10, 15, 20, 25, 30\}^\circ$, represented by different colors) and 3 different granular mass densities (1700, 2000, and 2500 kg/m^3, represented by symbols: circles, squares, and triangles, respectively). m_f is fixed at 10^{-3} m^{-1}. In each subplot, Eq. 2 is used to fit all the reported scenarios (solid line), and the maximum and minimum (dashed lines) among the maximum wave heights (H) recorded for each volume across the parameter space. These fits provides best values and variability of $\alpha_{\log}$ and α_{ref} (reported in legend). The normalized fit error σ_χ and the relative difference σ_α are also reported in each subplot. When the fit is linear, both coefficients coincide. For each volume, the mean $\langle H(V)\rangle$ is displayed with a black cross

365 flow motion and more efficient energy transfer to the water (Poulain et al., 2023). Coefficients remain constant for most gauges (e.g., gauge 0: 10 cm at all volumes), but gauge 7 shows a decrease from $\alpha_{\log} \simeq 15$ cm per 10^6 m^3 to $\alpha_{\text{ref}} \simeq 6$ cm per 10^6 m^3, reflecting localized nonlinearity. The σ_χ values indicate that locations near the villages maintain relatively low variability (15.2 - 36.8%), while σ_α values remain high across the different locations (47.6 - 80.7%), suggesting that the coefficient α is highly sensitive to variations in m_f values.

370 In Figure 8, where the influence of m_f is analyzed for subaerial flows originating from position B0 (see Fig. 1), we observe different trends depending on gauge location. Near the SdF (gauges 0 and 1), higher m_f values result in higher H. Subaerial granular flows entering the water column benefit from stronger shear and mechanical coupling at higher m_f, facilitating more efficient momentum transfer. For example, gauge 0 shows the most pronounced increase in wave height as m_f increases: the maximum wave height for $m_f = 10^{-1}$ m^{-1} and $V = 30 \times 10^6$ m^3 reaches ~ 25 m, while for $m_f = 10^{-5}$ m^{-1}, it is ~ 10 m.
375 Offshore from the SdF (gauges 4 and 5), we observe the opposite trend. The higher coupling inhibits the ability of the granular flow to propagate along the sea bottom, resulting in a lower wave height in those locations, where the maximum value results from a single wave packet where dissipation has already merged the different peaks observed near the SdF (see Fig. 2). At

Stromboli village (gauges 7, 8, and 9) a mixed trend is observed, while at Ginostra the same trend observed in front of the SdF is maintained. Here, σ_χ (15.3 - 40.0%) is lower than in submarine cases (Fig. 7), although σ_α reaches 53.7 - 86.3%. This reflects an amplified uncertainty in coefficient estimates due to the nonlinear relationship between m_f and flow volume.

In Figure 9, we analyze the variability in wave amplitude for submarine granular flows originating from position B7 along the three distinct transects (northern, central, and southern axes, as shown in Fig. 1 and Table 1). The relationship between V and H remains nearly linear, although the initial elevation systematically influences wave amplitudes. For most gauges, flows originating from the central axis generate the largest amplitudes, followed by the southern lateral side, with the northern lateral side consistently producing the smaller wave amplitudes regardless of gauge location. Near the Stromboli village (gauges 7, 8, and 9), coefficients average $\alpha_{\text{lin}} \simeq 6$ cm per 10^6 m^3, compared to $\alpha_{\text{lin}} \simeq 9$ cm per 10^6 m^3 in front of the SdF. σ_χ values (32.9 - 44.4%) reflect moderate scatter around the linear fit, with the highest variability at gauge 7. σ_α values (21.6 - 63.1%) indicate significant variability in α_{lin} estimates. These uncertainties can be due to bathymetry effects, as the lateral flows from the northern and southern axes interact with the submerged borders of the SdF large scar, dissipating energy laterally.

In Figure 10, we examine subaerial granular flows originating from position B0 along the three distinct transects (see Fig. 1) and their nonlinear relationship with wave amplitude. In contrast with the systematic trends in the submarine cases (Fig. 9), subaerial wave amplitudes vary irregularly across transects and gauges. For example, around the villages (gauges 8, 9, and 10), the transect producing the largest amplitudes shifts with volume. This may be caused by bathymetric refraction and shoreline interactions modulating wave amplitudes. In front of the SdF, at gauge 0, flows from the southern axis with $V = 30 \times 10^6$m^3 generates waves over 30 m, while equivalent central/northern flows yield < 15 m. Coefficients in front of the SdF (gauges 0 and 1) exhibit an average value of $\alpha_{\log} \simeq 1.2$ m per 10^6 m^3 for $V < 10 \times 10^6$ m^3, decreasing to $\alpha_{\text{ref}} \simeq 40$ cm per 10^6 m^3 for $V > 10 \times 10^6$ m^3. In contrast, near the Stromboli village (gauges 7, 8, and 9), this value is $\alpha_{\log} \simeq 37$ cm per 10^6 m^3, further decreasing to $\alpha_{\text{ref}} \simeq 20$ cm per 10^6 m^3 for $V > 10 \times 10^6$ m^3. σ_χ indicate moderate to high variability (10.7 - 43.6%) across gauges, with the best fit at distal gauges. σ_α values (28.6 - 80.7%) are notably higher than those for submarine flows (Fig. 9), reflecting the nonlinear energy transfer at the impact.

4.4 Wave height dependence on source volume and elevation

For each extended dataset and each source elevation, we computed the best-fitting coefficients of the relation between H and V, allowing source density ρ and one secondary parameter (δ, m_f, or D) to vary. In addition to the central (best-fit) coefficient, we also determined the maximum and minimum coefficients across all parameter combinations. Examples of these fits (best, max, and min) are shown in Figs. 5-10. We then plotted the resulting coefficients as a function of submergence depth s for each gauge; these plots for both submarine and subaerial scenarios are provided in the Supplementary Material (Figs. S19–S24). To combine information from all datasets using the same weight, we averaged the best-fit coefficients to obtain a single representative value, and used extreme coefficient values to define an uncertainty band.

In the submarine case, the dependence of H on V in well described by Eq. 1 where the coefficient α itself decays exponentially with submergence depth (Eq. 4). Figure 11 shows the best-fit coefficients (red dots) and their max-min ranges (shaded bars) versus s, together with exponential fits (black lines) all using a fixed e-folding depth $s_0 = 191$ m. The fitted values of

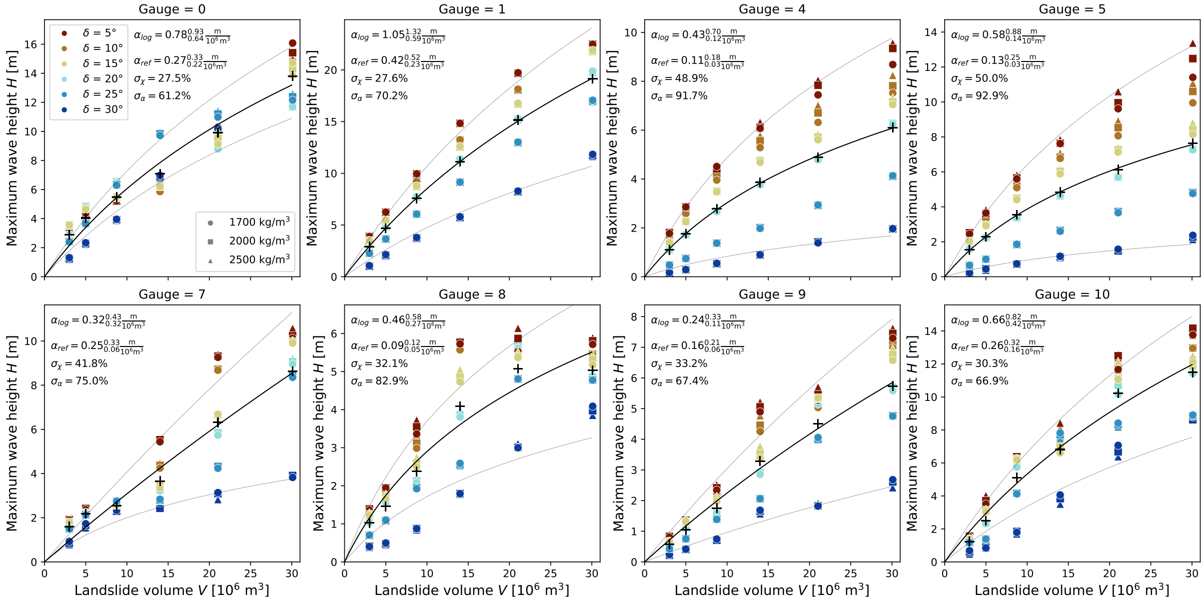

Figure 6. Variability of the maximum wave height as a function of the landslide volume for a fixed subaerial starting elevation (B0, see Fig. 1). The results are shown for different friction angles ($\delta_1 = \delta_3 = \{5, 10, 15, 20, 25, 30\}^\circ$; colors) and densities (1700, 2000, and 2500 kg/m^3; symbols) with m_f fixed at 10^{-3} m^{-1}. In each subplot, Eq. 2 is used to fit all the reported scenarios (solid line), and the maximum and minimum (dashed lines) among the maximum wave heights (H) recorded for each volume across the parameter space. These fits provides best values and variability of α_{log} and α_{ref} (reported in legend). The normalized fit error σ_χ and the relative difference σ_α are also reported in each subplot. A logarithmic trend is observed for all gauges, causing the slopes of the fit at $V = 0$ (α_{log}) and $V = 30 \times 10^6\,\text{m}^3$ (α_{ref}) to differ. For each volume, the mean $\langle H(V) \rangle$ is displayed with a black cross

α_0 for the central, maximum, and minimum cases are reported in the legend and in Table 3). Thus our proposed 2-parameter model for submarine sources is

$$H(V, s) = \alpha_0 e^{-s/s_0}\, V\,. \tag{5}$$

For subaerial sources, a logarithmic relation (Eq. 2) captures the volume dependence more accurately. It is characterized by the 2 coefficient parameters α_{log} (in $V = 0$ m^3) and α_{ref} (in $V = 3 \cdot 10^7$ m^3). Figure 12 shows α_{log} (red) and α_{ref} (blue) versus submergence $s = -q$ ($s < 0$ in the subaerial case), with dots for best-fits and shaded bars for their max-min ranges. Horizontal lines mark the weighted averages (see legends and Table 3). Unlike the submarine case, the dependence on s is weaker for subaerial sources, thus our proposed 2-parameter model for these sources is Eq. 2. These 2 coefficients differ significantly, underlining the variability one would obtain from a simple linear approximation for all volumes. In particular, any equivalent linear coefficient α_{lin} would lie between α_{ref} and α_{log}, being larger than the former and smaller than the latter.

Finally, we note that these empirical fits are consistent with the insights from our Sobol sensitivity analysis (Section 4), reinforcing confidence in both the proposed parameterizations and overall methodology.

https://doi.org/10.5194/egusphere-2026-1757
Preprint. Discussion started: 10 April 2026

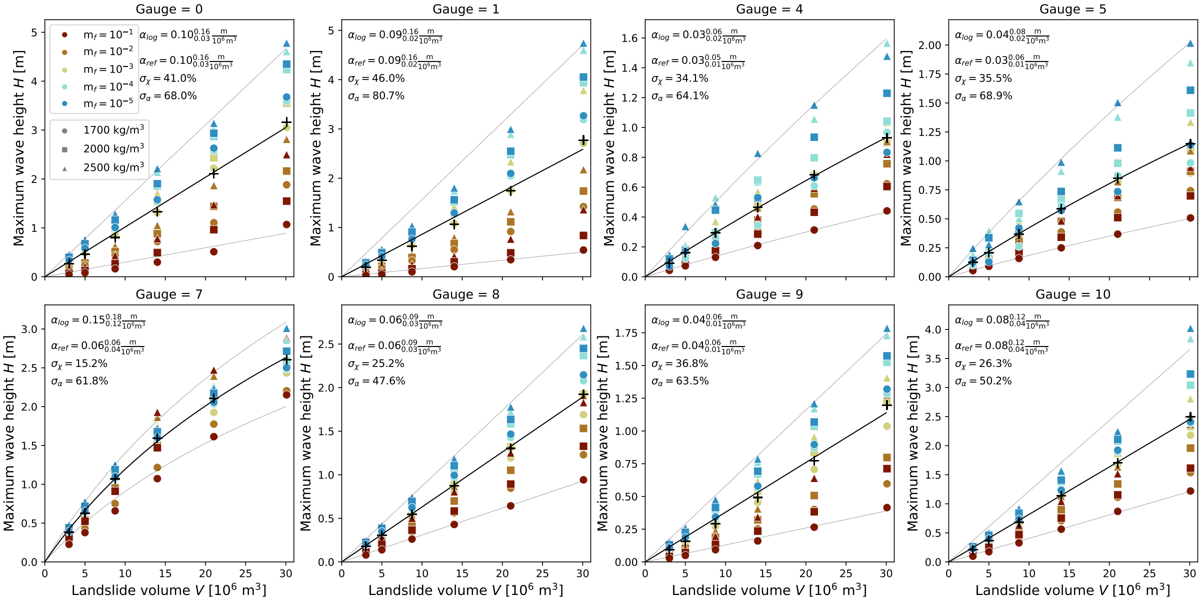

Figure 7. Variability of the maximum wave height as a function of the landslide volume for a fixed submarine elevation (B7, see Fig. 1). The wave height is shown for 5 different configurations of m_f ($10^{-1}, 10^{-2}, 10^{-3}, 10^{-4}, 10^{-5}$ m^{-1}, represented by different colors) and 3 different granular mass densities (1700, 2000, and 2500 kg/m^3, represented by symbols: circles, squares, and triangles, respectively). δ_1 is fixed at 15°. In each subplot, Eq. 2 is used to fit all the reported scenarios (solid line), and the maximum and minimum (dashed lines) among the maximum wave heights (H) recorded for each volume across the parameter space. These fits provides best values and variability of α_{log} and α_{ref} (reported in legend). The normalized fit error σ_χ and the relative difference σ_α are also reported in each subplot. The slopes of the fit of the wave height are reported at $V = 0$ and $V = 30 \times 10^6$ m^3 (α_{log} and α_{ref}, respectively). When the fit is linear, both coefficients coincide. For each volume, the mean $\langle H(V) \rangle$ is displayed with a black cross

5 Discussion

5.1 Sensitivity analysis of slide parameters

It has been demonstrated across multiple experimental, statistical, and numerical studies that key landslide parameters for the generation of tsunamis commonly include volume, velocity, and initial acceleration of the sliding mass (Fritz et al., 2004; Løvholt et al., 2005; Harbitz et al., 2006; Sarri et al., 2012; Løvholt et al., 2015; Macías et al., 2015; Urgeles et al., 2019; Zhao et al., 2021; Pedrosa-González et al., 2022; Bougouin et al., 2024). Early parametric studies identified landslide volume as a first-order feature in contributing to tsunami amplitude, with larger volumes generating higher waves (Løvholt et al., 2005; Harbitz et al., 2006). For instance, Løvholt et al. (2005) demonstrated that submarine slides in the Storegga region produced tsunami heights proportional to their volume and initial acceleration (or maximum velocity). Our Sobol sensitivity analysis, performed on the combined dataset of subaerial and submarine granular flows, also highlights the importance of volume with an average normalized total index of $\sim 20\%$, while identifying the initial flow elevation (i.e., the distinction between subaerial

https://doi.org/10.5194/egusphere-2026-1757
Preprint. Discussion started: 10 April 2026

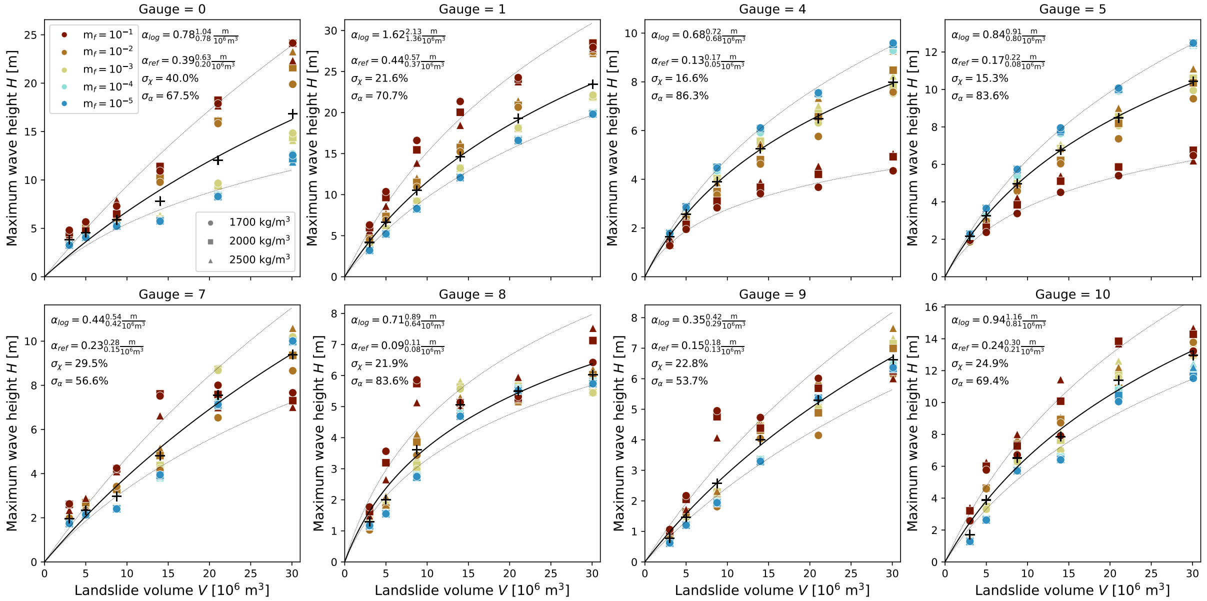

Figure 8. Variability of the maximum wave height as a function of the landslide volume for a fixed subaerial starting elevation (B0, see Fig. 1). The results are shown for different m_f ($10^{-1}, 10^{-2}, 10^{-3}, 10^{-4}, 10^{-5}$ m^{-1}; colors) and densities (1700, 2000, and 2500 kg/m^3; symbols) with δ_1 fixed at 15°. In each subplot, Eq. 2 is used to fit all the reported scenarios (solid line), and the maximum and minimum (dashed lines) among the maximum wave heights (H) recorded for each volume across the parameter space. These fits provides best values and variability of $\alpha_{\log}$ and α_{ref} (reported in legend). The normalized fit error σ_χ and the relative difference σ_α are also reported in each subplot. A logarithmic trend is observed for all gauges, causing the slopes of the fit at $V = 0$ ($\alpha_{\log}$) and $V = 30 \times 10^6\,\mathrm{m}^3$ (α_{ref}) to differ. For each volume, the mean $\langle H(V) \rangle$ is displayed with a black cross

Table 3. Parameters α for each Gauge (submarine and subaerial cases) with their ranges (min-max). Units are $\frac{\mathrm{m}}{10^6\,\mathrm{m}^3}$. Additionally, $V_{\log}/2$ is reported in $10^6\,\mathrm{m}^3$ as an indicator of the onset of the transition between the linear and logarithmic regimes. At $V = V_{\log}/2$, the local slope is $H'(V) = \frac{2}{3}\alpha_{\log}$ (equivalently, $\alpha_{\log}/H'(V) = 1.5$, see Eq. 3). Symbol $\nearrow$ indicates $\frac{1}{2}V_{\log} > 30 \cdot 10^6\,\mathrm{m}^3$.

Gauge	$\boldsymbol{\alpha_0}$ (submarine)	$\boldsymbol{\alpha_{\log}}$ (subaerial)	$\boldsymbol{\alpha_{\mathrm{ref}}}$ (subaerial)	$\frac{1}{2}\boldsymbol{V_{\log}}$ (subaerial)
0	0.75 (0.18−1.04)	1.16 (0.64−3.32)	0.37 (0.17−1.05)	7.2 (2.3 − $\nearrow$)
1	0.60 (0.14−1.10)	1.33 (0.50−2.35)	0.48 (0.15−0.76)	9.0 (2.7 −26.3)
4	0.23 (0.05−0.54)	0.58 (0.11−1.12)	0.15 (0.02−0.25)	5.1 (1.2 − 7.7)
5	0.28 (0.07−0.64)	0.71 (0.14−1.41)	0.19 (0.02−0.38)	5.5 (1.2 −14.2)
7	0.35 (0.10−0.47)	0.40 (0.19−0.62)	0.28 (0.04−0.46)	$\nearrow$ (1.8 − $\nearrow$)
8	0.34 (0.05−0.46)	0.67 (0.27−0.98)	0.10 (0.04−0.16)	3.0 (1.1 − 5.9)
9	0.24 (0.04−0.39)	0.32 (0.11−0.54)	0.18 (0.06−0.24)	21.7 (8.2 − $\nearrow$)
10	0.52 (0.08−0.71)	0.81 (0.42−1.26)	0.25 (0.14−0.57)	7.0 (3.7 − $\nearrow$)

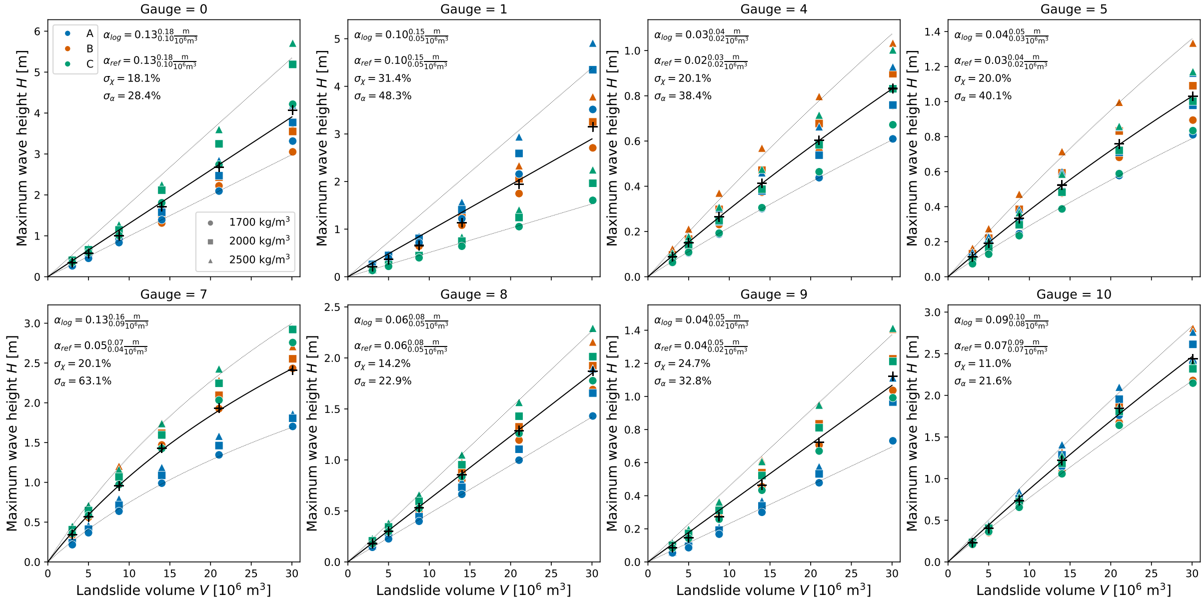

Figure 9. Variability of the maximum wave height as a function of the landslide volume for fixed submarine starting elevations along the 3 different transects (A7, B7, and C7 see Fig. 1, shown with different colors). The results are shown for different densities (1700, 2000, and 2500 $\mathrm{kg/m^3}$; symbols) with δ_1 and m_f fixed at 15° and $10^{-3}\ \mathrm{m^{-1}}$, respectively. In each subplot, Eq. 2 is used to fit all the reported scenarios (solid line), and the maximum and minimum (dashed lines) among the maximum wave heights (H) recorded for each volume across the parameter space. These fits provides best values and variability of α_{log} and α_{ref} (reported in legend). The normalized fit error σ_χ and the relative difference σ_α are also reported in each subplot. The slopes of the fit of the wave height are reported at $V = 0$ and $V = 30 \times 10^6\,\mathrm{m}^3$ (α_{log} and α_{ref}, respectively). When the fit is linear, both coefficients coincide. For each volume, the mean $\langle H(V) \rangle$ is displayed with a black cross

and submarine sources) as the dominant control on the relative sensitivity of H ($\sim 60\%$). Since in our simulations we model the dynamics of the source as a granular flow initially still and not with a prescribed kinematic law, flow velocity is not a free parameter, but depends on flow rheology, elevation and volume. Accordingly, sensitivity to these parameters also reflects the way they control granular flow velocity, acceleration, and spreading across the SdF.

When subaerial and submarine datasets are analyzed separately, results for subaerial slides suggest that the flow volume has the greatest influence on H, with an average normalized total index of $\sim 60\%$. This result is in line with those of recent experimental studies on granular collapses emphasizing landslide volume as the dominant control on tsunami generation, reflecting impulsive energy transfer at the air-water interface during granular impact (Huang et al., 2020; Robbe-Saule et al., 2021b, a). Notably, the initial elevation of the granular flow along the SdF has a minimal relative importance ($\sim 3\%$), indicating that maximum wave heights are quite insensitive to failure locations along the slope. The limited influence of q on H may appear counterintuitive, as higher elevation failures have greater potential energy. However, landslides initiating from elevated positions undergo increased spreading and frictional dissipation as they travel downslope, forming a long sediment tail and

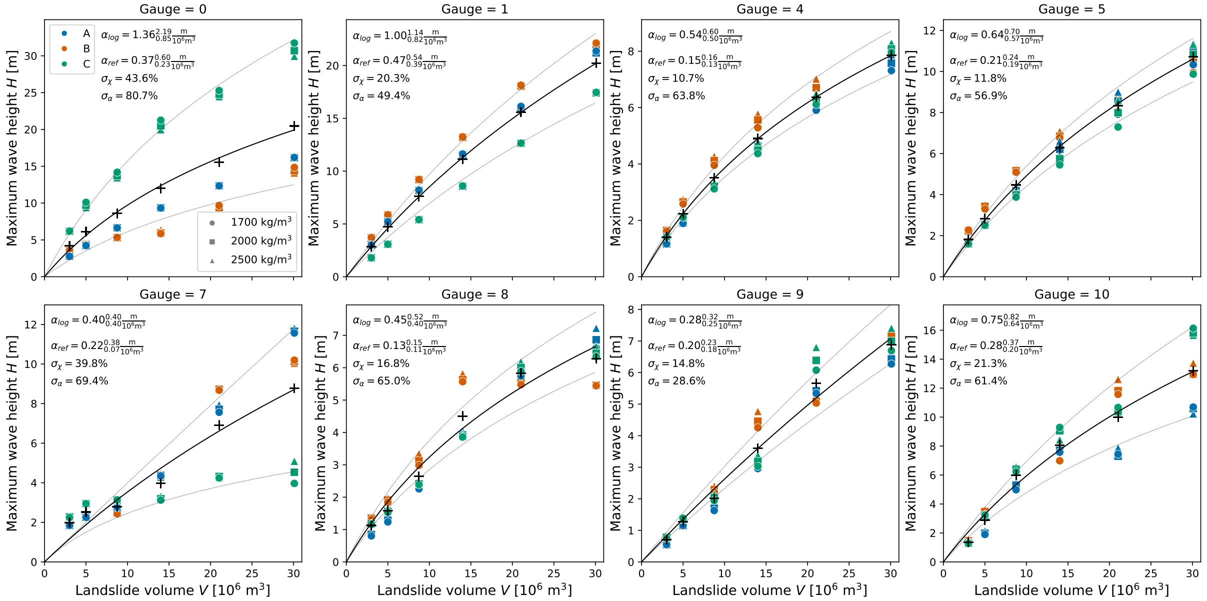

Figure 10. Variability of the maximum wave height as a function of the landslide volume for fixed subaerial starting elevations along the 3 different transects (A0, B0, and C0 see Fig. 1, shown with different colors). The results are shown for different densities (1700, 2000, and 2500 kg/m^3; symbols) with δ_1 and m_f fixed at 15° and 10^{-3} m^{-1}, respectively. In each subplot, Eq. 2 is used to fit all the reported scenarios (solid line), and the maximum and minimum (dashed lines) among the maximum wave heights (H) recorded for each volume across the parameter space. These fits provides best values and variability of α_{log} and α_{ref} (reported in legend). The normalized fit error σ_χ and the relative difference σ_α are also reported in each subplot. A logarithmic trend is observed for all gauges, causing the slopes of the fit at $V = 0$ (α_{log}) and $V = 30 \times 10^6$ m^3 (α_{ref}) to differ. For each volume, the mean $\langle H(V) \rangle$ is displayed with a black cross

reducing the effective volume entering the water at the time of the impact. This effect, however, can be locally mitigated by the presence of topographic incisions or channels, which can focus the granular flow, limit its lateral spreading, and maintain a higher momentum flux into the water column (Casalbore et al., 2025). Previous studies have concluded that the majority of energy transfer from the landslide to the free surface occurs very close to the time of impact (Heller et al., 2016; Clous and Abadie, 2019; Yavari-Ramshe and Ataie-Ashtiani, 2019). Accordingly, when different parts of the sliding mass move at different velocities and enter the sea at different times, the tsunamogenic power of the landslide at the impact area decreases. This effect becomes more pronounced as the distance traveled by the slide increases. We also report a relatively strong influence of δ on H ($\sim 22\%$), with localized contributions exceeding $\sim 46\%$ at offshore gauges. Frictional resistances of the sliding material can greatly reduce the flow impact velocity and its effective mass (to around 10-40% of the initial material), resulting in a less vigorous impact and a smaller wave (Yavari-Ramshe and Ataie-Ashtiani, 2019). The pronounced sensitivity of δ at offshore gauges can be due to dispersive wave trains amplifying friction-driven variations in landslide dynamics through phase-dependent constructive interference, affecting H. In contrast, nearshore gauges can experience wave breaking, reflection, and shoaling effects, which homogenize sensitivity by dissipating variations driven by δ. The other dissipation term, m_f, and the

https://doi.org/10.5194/egusphere-2026-1757
Preprint. Discussion started: 10 April 2026

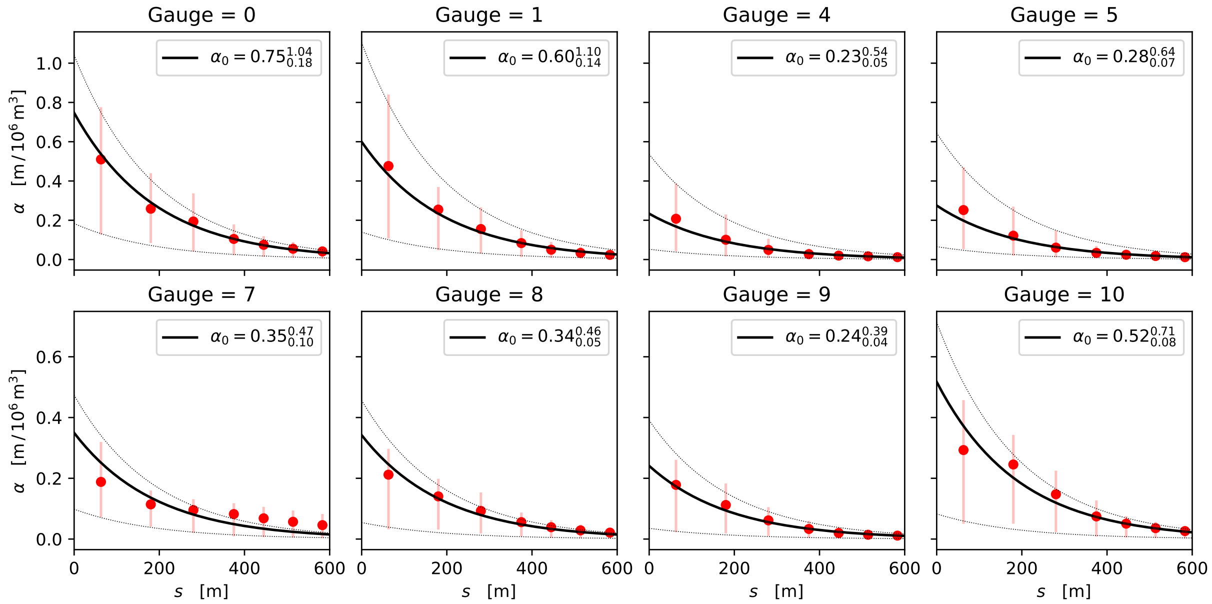

Figure 11. Dependence of the linear coefficient α on submergence depth s for submarine sources. Red dots denote best-fit coefficients; shaded red bars indicate the range between the maximum and minimum coefficients, across the whole parameter variations (Tab. 1). Black curves are exponential fits (Eq. 4), all with $s_0 = 191$ m. Legend entries give the values of α_0 as obtained by fitting central, maximum and minimum coefficients

transect D appear to have a modest relative importance, with averaged values of $\sim 8\%$. It is interesting to note that the latter parameter shows a localized anomaly at gauge 0 ($\sim 30\%$), likely due to bathymetric modulation of tsunami waves. This gauge is located along the submerged canyon that mirrors the SdF incision, whereas nearby gauges outside the incision experience no such morphological focusing of the waves. Consistently with the analysis of Δ_k, non-additive effects in the subaerial subset are limited to a few percent, indicating that the response is close to additive and that the dominant role of V is not strongly coupled with source elevation.

In contrast, submarine flows exhibit balanced sensitivity between volume ($\sim 37\%$) and initial elevation ($\sim 35\%$). Our findings corroborate those of Snelling et al. (2020), who conducted a probabilistic sensitivity analysis using smooth particle hydrodynamics simulations and found that landslide volume and initial submergence depth are the dominant parameters influencing maximum wave heights. Similarly, Cabrera et al. (2020), using an experimental apparatus, demonstrated that at higher submergence ratios, submarine collapses generate both seaward and landward waves, with seaward wave amplitudes having an inverse relation with submergence depth (elevation) and landward waves correlating with column geometry (volume). This dual dependence aligns with our results, which show that H associated with submarine granular collapses is mostly governed by the combined influence of q and V. Nguyen (2022) also found that the relative submerged depth (i.e., the ratio of initial granular height to water depth) is a critical factor controlling H in submarine granular collapses, further highlighting the importance of elevation-dependent mechanisms in such scenarios. Compared to subaerial flows, δ contributes less to overall relative sensitiv-

https://doi.org/10.5194/egusphere-2026-1757
Preprint. Discussion started: 10 April 2026

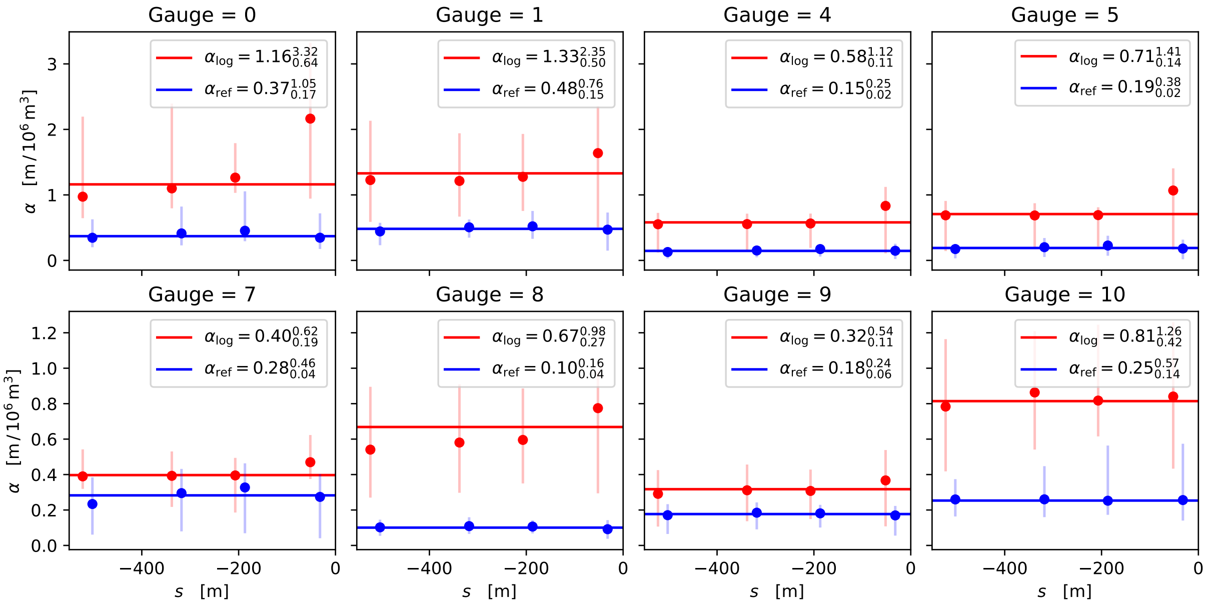

Figure 12. Volume dependence coefficients for subaerial sources as functions of submergence $s = -q$. Red dots and bars show the best-fit values and their max-min ranges for α_{log} (coefficient at $V \to 0$); blue dots and bars show those for α_{ref} (value at $V_{\text{ref}} = 3 \cdot 10^7$ m^3). Horizontal lines give their averages (values in legends).

ity in submarine cases ($\sim 18\%$), although its localized influence remains notable at offshore gauges (up to $\sim 36\%$). Similar to subaerial dynamics, δ governs slide acceleration and runout distance by modulating basal friction during downstream propagation, an effect that appears to be amplified at offshore gauges. These findings suggest that, while flow elevation and volume dominate submarine slide-generated waves, δ remains a secondary yet non-negligible factor in wave dynamics. Like in subaerial scenarios, m_f and D contribute modestly to relative sensitivity in submarine cases, although their influence is slightly lower than in subaerial counterparts. The low contribution of m_f on the generated waves has been also observed in numerical simulations by Poulain et al. (2022) for typical values of m_f between 0 and 10^{-4} m^{-1}. In this subset, however, the values of Δ_k indicate that non-additive effects increase again to about 6–10%, with q and, when included, δ being the parameters most strongly involved. This suggests that, for submarine sources, the effect of source elevation is more strongly coupled with the other controls on wave generation.

Although velocity and initial acceleration are widely recognized as key factors in tsunami generation (e.g., Løvholt et al., 2005), our sensitivity analysis does not explicitly include these parameters. Instead, variations in velocity are implicitly controlled by the initial flow elevation along the SdF slope, which determines the gravitational potential energy driving acceleration, and by friction angles, which modulate deceleration during seaward propagation. Thus, although velocity and acceleration are not direct inputs in our sensitivity analysis, their effects are indirectly captured through the interplay of elevation, volume, and friction parameters, which dominate sensitivity in our scenarios at Stromboli. More precisely, they are captured through the additive and non-additive effects associated with these parameters.

Our Sobol analysis also shows that, regardless of the initial position of propagation (subaerial vs. submarine), the bulk density of granular flows has a negligible effect on H ($< 0.2\%$), consistent with previous works (Robbe-Saule et al., 2021a; Nguyen, 2022; Bougouin et al., 2024; Esposti Ongaro et al., 2025). For instance, Bougouin et al. (2024) found that even large density variations in pyroclastic flows (e.g., bulk density increases from 900 to 3000 kg m^3) modulate tsunami amplitudes by only a factor of 3-4. As demonstrated in their empirical scaling laws, this effect is minimal compared to variations in wave amplitude driven by changes in volume or velocity, which in their study spanned much wider ranges and led to amplitude fluctuations across several orders of magnitude. Robbe-Saule et al. (2021a) also highlighted that the effect of the density of the grains on the wave amplitude is negligible, indicating that the volume of the granular material plays a more crucial role than its mass. In our case, the role of ρ is negligible not only in terms of normalized total sensitivity, but also in terms of non-additive effects, confirming that density is a truly minor control on H within the range of values explored here.

The Sobol analysis further indicates that non-additive effects are almost entirely dominated by second-order contributions, whereas third-order and higher-order terms are negligible, with contributions of the order of 1%. This implies that departures from a purely additive response arise mainly from pairwise couplings between parameters, while more complex dependencies play only a marginal role.

5.2 Volume-wave scaling relationships and hazard implications

Our numerical results indicate distinct scaling relationships between V and H for subaerial and submarine sources. For submarine flows, the correlation is near-linear, whereas for subaerial flows, it follows a logarithmic trend. This pattern holds when varying δ, m_f, and D. This difference may be ascribed to the different physical mechanisms governing energy transfer in the two environments.

Subaerial flows exhibit a logarithmic relationship between V and H, with no significant dependence on the initial submergence depth, thereby mimicking the low sensitivity of this parameter found in the Sobol analysis. As the volume of the granular mass increases, the efficiency of momentum transfer to the water diminishes. The mechanisms for such a reduced efficiency at larger volumes deserves a more thorough investigation, but it is likely due to topographic spreading and localized dissipation during the descent, which limit the direct transfer of momentum into the water, leading to a logarithmic scaling between V and H. As we already mentioned, the transfer of energy between the slide and the water is very quick (Heller et al., 2016; Clous and Abadie, 2019; Yavari-Ramshe and Ataie-Ashtiani, 2019). Lower-elevation slides are more capable of conveying their energy into water as they are less affected by spreading and dissipation processes during their movement downslope. Consequently, subaerial slides have an optimal initial location close to the shorelines (positions A3, B3, and C3 in Fig. 1), which produces the largest tsunami waves, a phenomenon also observed in previous studies (Fine et al., 2003; Yavari-Ramshe and Ataie-Ashtiani, 2019; Esposti Ongaro et al., 2025). In contrast, submarine flows show a linear relationship with V, where the wave generation efficiency decays exponentially with submergence depth. The direct coupling between the sliding mass and the water column

https://doi.org/10.5194/egusphere-2026-1757
Preprint. Discussion started: 10 April 2026

results in a proportional increase in wave height with V, but this effect is progressively damped with increasing depth, likely due to water loading and geometric dispersion.

The quantitative relationships between landslide volume, submergence depth, and maximum tsunami wave height derived in this study provide a potential tool for preliminary hazard assessment. The distinct behaviors shown in Fig. 13 form the basis for a simplified methodology, a framework built on the key parameter α (i.e., the maximum wave height in meters, per million of cubic meters of the landslide) that offers a compromise between the inherent variability of the phenomenon and the need for rapid applicability. For subaerial sources (blue curve in Fig. 13), the wave height dependence on volume is best described by a logarithmic function (Eq. 2), that we have characterized with two coefficients. The coefficient α_{log}, captures the nearly linear behavior for volumes up to 5–10×10^6 m^3. However, using α_{log} for larger volumes leads to an overestimation of the wave height. Therefore, for conservative estimates, the linear approximation with α_{log} is valid, while for accuracy across the entire volume range, the full two-parameter logarithmic function requiring both α_{log} and α_{ref} is necessary. For submarine sources (black curves in Fig. 13), the wave height maintains a linear relationship with V, but the coefficient α decays exponentially with submergence depth s (Eq. 4). The exponential decay for submarine landslides is characterized by the e-folding depth $s_0 = 191$ m, which, notably, assumes a constant value regardless the gauge location. This value indicates that the tsunami-generating potential of a submarine landslide at Stromboli decreases by a factor of $\sim 1/e$ (approximately 37%) for every ~ 200 m of increased submergence. This scale is linked to the specific bathymetry of the SdF, reflecting the depth over which the energy transfer from the moving granular flow to the water column becomes significantly less efficient due to increased hydrostatic pressure and geometric dispersion. This finding indicates that slides initiating beyond a depth of a few hundred meters have a rapidly diminishing tsunamigenic potential for a given volume compared to their shallower counterparts. Analogous to the subaerial case, the simplest conservative approach is to use the value α_0 (the extrapolated coefficient at the shoreline), which overestimates wave height for any submerged source. For greater precision, the two-parameter model (Eq. 5) should be used, incorporating the characteristic depth s_0.

A key finding is the crossover in hazard potential between subaerial and submarine granular flows shown in Fig. 13. For small volumes ($< 10 \times 10^6$ m^3), subaerial slides tend to produce higher waves ($\alpha_{\text{log}} > \alpha_0$). However, for larger volumes, this trend reverses, and submarine slides can generate larger waves per unit volume due to the persistent linear relationship, unlike the logarithmic saturation in subaerial cases. This is justified by the fact that large subaerial flows experience significant energy dissipation and thinning as they travel down the volcanic flank before impacting the water. In contrast, submarine slides transfer energy to the water column simultaneously with their movement, resulting in a more efficient generation mechanism for very large volumes.

As a practical application, we use Fig. 13 to estimate the volume of the 2002 landslide at Stromboli that generated a ~ 10 m wave observed at gauge 8. Applying our submarine model (Eq. 5 with $\alpha_0 = 0.34$ m$/10^6$ m^3) yields an estimated landslide volume of $\sim 29 \times 10^6$ m^3, which is consistent with the upper-range reconstruction by Fornaciai et al. (2019). For comparison, using the average subaerial model would require a volume of $\sim 84 \times 10^6$ m^3. However, using the maximum values of α_{log} and α_{ref} from the uncertainty range for subaerial slides reduces the required volume to $\sim 28\times10^6$ m^3, while the maximum value for the submarine model would require only $\sim 22\times10^6$ m^3. This latter estimate is in good agreement with the most widely accepted reconstructions of the 2002 submarine landslide volume, which is estimated to be $\sim 20 \times 10^6\,\mathrm{m}^3$ (e.g., Fornaciai et al., 2019). This correspondence suggests that the 2002 tsunami was likely generated by a landslide whose physical parameters (such as low basal friction or, equivalently, high velocity) maximized the transfer of momentum to the water column. Indeed, the alignment of the 2002 event with the upper bound of our predicted range reflects the systematic dependence observed in our simulations, where the lowest friction angles consistently produce the highest wave responses for any given volume (see Figs. 5, 6). Although our analysis confirms that δ significantly modulates H, this parameter is purposely omitted from the final scaling equations. This choice is driven by the difficulty of constraining rheological parameters from observations. By focusing on volume and elevation, which are primary controls and more easily estimated via remote sensing, we provide a more applicable tool for rapid hazard assessment. The influence of δ is instead implicitly captured by the upper and lower bounds of our fits. The comparison with the 2002 event highlight the importance of selecting the appropriate model and considering parameter uncertainties in hazard analysis. In this framework, the charts provided in Fig. 13 serve as a practical tool for estimating V from H, and viceversa. Specifically, these plots function as nomograms that allow for the estimation of the expected range of maximum wave heights for a given slide volume, or conversely, for the rapid inversion of source volumes from observed wave data.

Our finding on subaerial flows is supported by Poulain et al. (2023), who used the HySEA model to simulate flank collapses on Montagne Pelée volcano involving a wide range of volumes. They found that the wave amplitude increases logarithmically with increasing volume. In contrast, Tinti et al. (2008) simulated submarine landslides outside the SdF at Stromboli and found a power-law relationship between the landslide potential energy and the tsunami total energy. They concluded that an increase in the potential energy of the slide by one order of magnitude leads to a roughly two order of magnitude increase in the tsunami energy. This discrepancy with our results arises because their analysis is based on quantities integrated over the entire simulated domain, which do not constrain local measurements. This highlights that global energy assessments and local wave measurements capture different aspects of the tsunami generation process. In a recent experimental study, Robbe-Saule et al. (2021a) examined the generation of waves by the gravity-driven collapse of a subaerial granular column into a water layer of constant depth in a quasi two-dimensional configuration. They found that the maximum near-shore wave amplitude scales linearly with the landslide volume. This linear correlation contrasts with our logarithmic scaling observed in subaerial cases, likely because of the range of volumes they have used and because their experimental conditions do not account for the complex bathymetry and three-dimensional effects inherent to the natural prototype, which can significantly influence momentum transfer and energy dissipation.

A key question is the extent to which these scaling relationships can be generalized to other volcanic islands. While our quantitative results are modulated by the steep topo-bathymetry of the SdF, the identified physical trends likely represent a general feature of landslide-generated tsunamis. The dominance of V and q as primary controls is consistent with the general behavior of gravity-driven mass movements and their associated wave generation across various scales. In particular, the logarithmic saturation observed for subaerial flows is a signature of the energy dissipation and morphological spreading that occurs when a subaerial mass impacts the water surface. We expect this behavior to be a robust feature for any volcanic island with steep, open flanks (e.g., Anak Krakatau, Heidarzadeh et al. (2020), Montagne Pelée volcano, Poulain et al. (2023)), where

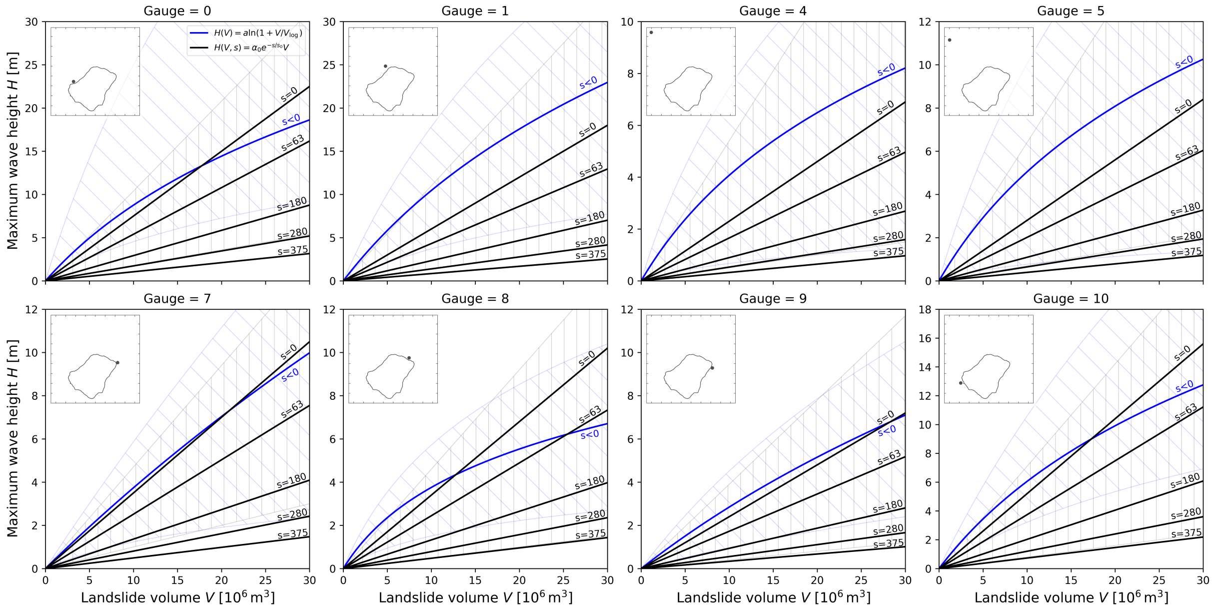

Figure 13. Maximum wave height as a function of landslide volume at different gauge locations. The blue curve shows the logarithmic relationship (Eq. 2) for subaerial landslides (s < 0). The black curves represent the linear relationship with exponential depth decay (Eq. 5) for submarine landslides at different submergence depths (s = 0, 63 m, etc.), showing reduced wave generation efficiency with increasing depth. Note the crossover point where submarine landslides of sufficient volume can generate larger waves than subaerial ones of the same volume. Blue diagonal hatching denotes the variability range for subaerial cases, whereas black vertical hatching denotes the corresponding range for submarine cases

the effective tsunamigenic mass is limited by the stretching and thinning of the flow during its subaerial transit, provided that topographic channeling does not significantly restrict horizontal spreading. Conversely, the linear volume scaling for submarine events, modulated by an exponential decay with depth, reflects a more direct momentum transfer. While s_0 depends on the local slope and the non-hydrostatic dispersion, the exponential form likely describes a universal decay of coupling efficiency as the water column thickness increases. From a methodological point of view, defining a local parameter α at relevant locations around the island proves to be a viable and efficient approach to directly link H with source characteristics. While the absolute values of α are site-specific, the underlying methodology remains widely applicable. By performing a constrained set of reference simulations for a given volcanic island, local α coefficients can be calibrated to construct predictive frameworks similar to those presented in Fig. 13. This is possible because the established functional forms require only a limited number of data points to constrain local scaling coefficients, effectively bypassing the need for exhaustive parametric exploration.

https://doi.org/10.5194/egusphere-2026-1757
Preprint. Discussion started: 10 April 2026

6 Conclusions

This study presents a comprehensive sensitivity analysis of tsunami generation by granular flows at Stromboli volcano, using an extensive set of numerical simulations to explore a 6-dimensional parameter space across wide ranges. Our results establish a clear hierarchy of influencing parameters: the granular flow initial submergence depth (elevation) and volume are the dominant controls on maximum wave height, while rheological properties play an important secondary role. More specifically, the relative sensitivity of the maximum wave height is dominated by source elevation when subaerial and submarine scenarios are analyzed together, whereas volume becomes dominant when only subaerial cases are considered, and volume and elevation have a more balanced role in submarine cases. Based on the sensitivity results, we identified and quantified two distinct scaling laws: a linear relationship with volume for submarine slides and a logarithmic relationship for subaerial slides. In addition, the efficiency of wave generation was found to decrease exponentially with submergence depth in submarine sources. The sensitivity analysis also shows that non-additive effects are essentially limited to second-order contributions, while third-order and higher-order terms are negligible, at the level of about 1%. This further supports the robustness of the proposed framework, as the dependence of maximum wave height on the input parameters is governed mainly by additive effects and pairwise couplings.

These findings not only reinforce our understanding of the underlying physics but also offer a practical, quantitative framework for hazard assessment. By providing the scaling parameters α, which measures how many meters of wave are expected for each million m^3 of mobilized material, our work effectively bridges the gap between complex numerical simulations and rapid field evaluations. The observed crossover in hazard potential, where subaerial slides are more hazardous than submarine ones for smaller volumes but submarine slides become relatively more hazardous for larger events, is a critical insight for emergency planning. At the same time, the sensitivity analysis shows that density has a negligible role, both in terms of relative sensitivity and non-additive effects, whereas frictional parameters may become locally important, especially at offshore gauges. Building on the approach of Esposti Ongaro et al. (2021, 2025), our models provide a physically-constrained dataset that can directly support probabilistic tsunami hazard analysis for Stromboli. The successful application of our scaling relations to estimate the volume of the 2002 event, yielding results consistent with the reconstruction by Fornaciai et al. (2019), further validates their utility. While the specific coefficients α_{log}, α_{ref}, α_0, and s_0 are calibrated for specific locations around Stromboli, the identified functional relationships, logarithmic for subaerial and linear-exponential for submarine sources, likely represent a general feature of landslide-generated tsunamis. Although the numerical values of these coefficients are site dependent, the separation between subaerial and submarine source regimes is identified as a key requirement for a physically meaningful interpretation of sensitivity and scaling behavior. This framework provides an efficient and scalable template for rapid hazard assessment at other volcanic islands, where local α coefficients can be calibrated using a limited set of reference simulations to bypass exhaustive parametric studies. Ultimately, this work provides a robust foundation for reconstructing past events and for delivering timely forecasts of tsunami impact based on initial observations of a landslide's location and estimated volume.

Code availability. The simulations presented in this study were carried out using the Multilayer-HySEA code. The source code is publicly available at the GitHub repository: https://github.com/edanya-uma/Multilayer-HySEA

Data availability. The numerical database supporting this research, including input source parameters and full simulated tsunami waveforms for all scenarios, is openly available on Zenodo at: 10.5281/zenodo.19222178

Appendix A: Empirical rheological models

In Multilayer HySEA (González-Vida et al., 2019; Macías et al., 2021b), the friction stress acting on the granular flow is composed by two contributions: (i) a Coulomb type law based on the Pouliquen and Forterre (2002) friction coefficient parametrization (stress τ_{g}); (ii) the friction between the water and the granular layers, defined as a particular case of the parametrization proposed in Pitman and Le (2005); Pelanti et al. (2008) (stress term τ_{wg}). In formula, the shallow water momentum equation of the granular layer has the following form:

$$\mathrm{d}_t(h_{\mathrm{g}}\mathbf{u}_{\mathrm{g}}) = \cdots + \tau_{\mathrm{g}} + \tau_{\mathrm{wg}}\,, \tag{A1}$$

where h_{g} and $\mathbf{u}_{\mathrm{g}}$ are the granular flow thickness and velocity, respectively.

A1 Friction of the granular flow

The Coulomb-type friction term τ_{g} in Eq. (A1) characterizes the internal frictional resistance within the granular layer. This stress opposes the flow direction and depends on the friction coefficient μ, which varies dynamically with flow thickness h_{g} and velocity magnitude $|\mathbf{u}_{\mathrm{g}}|$. Following the empirical formulation of Pouliquen and Forterre (2002), μ is defined through a regime-dependent function of the granular Froude number $\mathrm{Fr} = |\mathbf{u}_{\mathrm{g}}|/\sqrt{(1-r)gh_{\mathrm{g}}}$, with specific functional forms for subcritical ($\mathrm{Fr} < \beta$) and supercritical ($\mathrm{Fr} \geq \beta$) flow regimes. The coefficient μ transitions between two thickness-dependent functions: μ_{start}, representing the static friction at flow initiation, and μ_{stop}, describing the dynamic friction when the flow is moving. The specific forms of these terms are given by:

$$\tau_{\mathrm{g}} = -g\,r(1-r)\,\mu\,h_{\mathrm{g}}\frac{\mathbf{u}_{\mathrm{g}}}{|\mathbf{u}_{\mathrm{g}}|} \tag{A2}$$

$$\mu(h_{\mathrm{g}}, |\mathbf{u}_{\mathrm{g}}|) = \begin{cases} \mu_{\mathrm{start}}(h_{\mathrm{g}}) + \left(\frac{\mathrm{Fr}}{\beta}\right)^{\gamma}(\mu_{\mathrm{stop}}(h_{\mathrm{g}}) - \mu_{\mathrm{start}}(h_{\mathrm{g}})) & \text{for } \mathrm{Fr} < \beta \\ \mu_{\mathrm{stop}}\left(\frac{\beta}{\mathrm{Fr}}h_{\mathrm{g}}\right) & \text{for } \mathrm{Fr} \geq \beta \end{cases} \tag{A3}$$

$$\begin{cases} \mu_{\mathrm{start}}(h) = \tan(\delta_3) + (\tan(\delta_2) - \tan(\delta_1))\dfrac{1}{1 + h/\ell} \\ \mu_{\mathrm{stop}}(h) = \tan(\delta_1) + (\tan(\delta_2) - \tan(\delta_1))\dfrac{1}{1 + h/\ell} \end{cases} \tag{A4}$$

https://doi.org/10.5194/egusphere-2026-1757
Preprint. Discussion started: 10 April 2026

Here, g is gravity and r is the water to granular density ratio. This law has 3 empirical parameters: $\beta = 0.136$; $\gamma = 10^{-3}$, and $\ell = 1$ m. The three characteristic angles of the granular material are δ_1, δ_2, δ_3, with $\delta_1 \leq \delta_3$ and $\delta_2 \geq \delta_1$.

The behavior of the law can be described by looking at the different possible regimes:

- If $\mathrm{Fr} \ll \beta$, then $\mu = \mu_{\text{start}}$, which is the static friction coefficient. When the granular material is at rest, if external forces on the point surpass the stress determined by this coefficient the layer starts to move.
- As $\mathrm{Fr} \to \beta$ the friction coefficient decreases continuously from the static coefficient to the dynamic coefficient $\mu_{\text{stop}}(h_{\text{g}})$. The shape of this transition is controlled by γ. Since γ is very small this transition is practically immediate as the flow starts to move.
- If the flow is thick ($h_{\text{g}} \gg \ell$), then both the static and dynamic friction coefficient behave as in the Coulomb case, with typical angles δ_3 and δ_1, respectively.
- If the flow is thin ($h_{\text{g}} \ll \ell$), then the dynamic friction angle increases to δ_2, and the static friction coefficient to $\mu_{\text{start}} = \tan(\delta_3) + (\tan(\delta_2) - \tan(\delta_1))$.
- In the dynamic case, if the flow is slow or thick enough to have $\frac{\mathrm{Fr}}{\beta} \ll \frac{h_{\text{g}}}{\ell}$, then the friction angle is δ_1. In the opposite case, if the flow is fast or thin and $\frac{\mathrm{Fr}}{\beta} \gg \frac{h_{\text{g}}}{\ell}$, the friction angle increases to δ_2.

All these observations tell us that δ_3 and δ_1 are the static and dynamic friction angle when the granular layer is thick enough. When $\delta_2 > \delta_1$, these angles increase (and with them the friction coefficient) as the flow increases its velocity or decreases its thickness. The transition velocity between these low-friction and high-friction regimes depends on the flow thickness in the following way:

$$u = \frac{\beta}{\ell}\sqrt{(1-r)g}\,h^{\frac{3}{2}}\,. \tag{A5}$$

An example illustrating the here described friction coefficient is reported in Supplementary Material (Fig. S25).

A2 Friction between water and the granular flow

The interfacial shear stress τ_{wg} in Eq. (A1) is modeled as a quadratic function of the relative shear velocity between the water and granular layers, following the parameterization in González-Vida et al. (2019):

$$\tau_{\text{wg}} = m_f \frac{r h_{\text{w}} h_{\text{g}}}{h_{\text{g}} + r h_{\text{w}}} (\mathbf{u}_{\text{w}} - \mathbf{u}_{\text{g}}) \|\mathbf{u}_{\text{w}} - \mathbf{u}_{\text{g}}\| \tag{A6}$$

where h_{w} and $\mathbf{u}_{\text{w}}$ are the thickness and depth-averaged velocity of the water layer, and m_f is the empirical friction coefficient between water and granular material, with dimensions m^{-1}.

This formulation captures the turbulent drag at the interface, which scales quadratically with the relative velocity. The term $\frac{r h_{\text{w}} h_{\text{g}}}{h_{\text{g}} + r h_{\text{w}}}$ acts as an effective thickness, weighting the contributions of both layers and accounting for the density contrast r. The coefficient m_f is the parameter governing the momentum exchange intensity. Higher values of m_f result in stronger coupling between the layers, while lower values permit greater relative motion.

Author contributions. MT: Conceptualization, Methodology, Formal analysis, Data curation, Software, Visualization, Writing – original draft, Writing – review and editing. MC: Conceptualization, Methodology, Formal analysis, Visualization, Software, Writing – original draft, Writing – review and editing, Resources, Supervision, Project administration. TEO: Conceptualization, Methodology, Writing – review and editing. MdMV: Conceptualization, Methodology, Writing – review and editing. AT: Conceptualization, Methodology, Writing – review and editing

Competing interests. The contact author has declared that none of the authors has any competing interests

Acknowledgements. This research was carried out in the frame of the Istituto Nazionale di Geofisica e Vulcanologia (INGV) projects "Rete Multiparametrica – Vulcani A3" (D.P. 74/2020) and Progetto DL50 "Centro Italia" – Ricostruzione (D.P. 76/2020).

References

Auker, M. R., Sparks, R. S. J., Siebert, L., Crosweller, H. S., and Ewert, J.: A statistical analysis of the global historical volcanic fatalities record, J. Appl. Volcanol., 2, https://doi.org/10.1186/2191-5040-2-2, 2013.

Barberi, F., Rosi, M., and Sodi, A.: Volcanic hazard assessment at Stromboli based on review of historical data, Acta Vulcanol., 3, 173–187, 1993.

Bevilacqua, A., Bertagnini, A., Pompilio, M., Landi, P., Del Carlo, P., Di Roberto, A., Aspinall, W., and Neri, A.: Major explosions and paroxysms at Stromboli (Italy): a new historical catalog and temporal models of occurrence with uncertainty quantification, Sci. Rep., 10, 17 357, https://doi.org/10.1038/s41598-020-74301-8, 2020.

Bougouin, A., Paris, R., Roche, O., Siavelis, M., and Pawlak Courdavault, A.: Tsunamis generated by pyroclastic flows: experimental insights into the effect of the bulk flow density, Bulletin of Volcanology, 86, 35, https://doi.org/10.1007/s00445-024-01704-0, 2024.

Brunet, M., Moretti, L., Le Friant, A., Mangeney, A., Fernández Nieto, E. D., and Bouchut, F.: Numerical simulation of the 30–45 ka debris avalanche flow of Montagne Pelée volcano, Martinique: from volcano flank collapse to submarine emplacement, Natural Hazards, 87, 1189–1222, https://doi.org/10.1007/s11069-017-2815-5, 2017.

Cabrera, M. A., Pinzon, G., Take, W. A., and Mulligan, R. P.: Wave generation across a continuum of landslide conditions from the collapse of partially submerged to fully submerged granular columns, Journal of Geophysical Research: Oceans, 125, e2020JC016 465, https://doi.org/10.1029/2020JC016465, 2020.

Calvari, S., Di Traglia, F., Ganci, G., Bruno, V., Ciancitto, F., Di Lieto, B., Gambino, S., Garcia, A., Giudicepietro, F., Inguaggiato, S., et al.: Multi-parametric study of an eruptive phase comprising unrest, major explosions, crater failure, pyroclastic density currents and lava flows: Stromboli volcano, 1 December 2020–30 June 2021, Front. Earth Sci., 10, 899 635, https://doi.org/10.3389/feart.2022.899635, 2022.

Casalbore, D., Di Traglia, F., Favalli, M., Fornaciai, A., Romagnoli, C., Civico, R., Ricci, T., Berardino, P., Borselli, L., Calabria, P., Calvari, S., Carlà, T., Casagli, N., Casu, F., Chiocci, F. L., De Cesare, W., De Luca, C., Del Soldato, M., Esposito, A. M., Esposito, C., Giudicepietro, F., Gracchi, T., Lanari, R., Macedonio, G., Monterroso, F., Natale, A., Nolesini, T., Perna, S., Petronelli, D., Rossi, G., and Stefanelli, C. T.: Very fast canyon formation and evolution along active volcanic flanks: A case from Stromboli Island, Geomorphology, 488, 109 961, https://doi.org/10.1016/j.geomorph.2025.109961, 2025.

Cerminara, M., Esposti Ongaro, T., de' Michieli Vitturi, M., Tadini, A., Trolese, M., Fornaciai, A., Nannipieri, L., and Rodriguez Galvez, J. F.: Simulated scenarios of volcanic mass movements and associated tsunamis at Stromboli (Aeolian archipelago, Tyrrhenian sea, Italy). version 1, https://doi.org/10.13127/stromboli/sciara_del_fuoco_tsunami, istituto Nazionale di Geofisica e Vulcanologia (INGV) [Data set], 2024.

Chiocci, F. L. and Ridente, D.: Regional-scale seafloor mapping and geohazard assessment. The experience from the Italian project MaGIC (Marine Geohazards along the Italian Coasts), Marine Geophysical Research, 32(1–2), 13–23, https://doi.org/10.1007/s11001-011-9120-6, 2011.

Clare, M. A., Yeo, I. A., Watson, S., Wysoczanski, R., Seabrook, S., Mackay, K., Hunt, J. E., Lane, E., Talling, P. J., Pope, E., Cronin, S., Ribó, M., Kula, T., Tappin, D., Henrys, S., de Ronde, C., Urlaub, M., Kutterolf, S., Fonua, S., Panuve, S., Veverka, D., Rapp, R., Kamalov, V., and Williams, M.: Fast and destructive density currents created by ocean-entering volcanic eruptions, Science, 381, 1085–1092, https://doi.org/10.1126/science.adi3038, 2023.

Clous, L. and Abadie, S.: Simulation of energy transfers in waves generated by granular slides, Landslides, 16, 1663–1679, https://doi.org/10.1007/s10346-019-01180-0, 2019.

Dawson, A. G., Dawson, S., Bondevik, S., Costa, P. J. M., Hill, J., and Stewart, I.: Reconciling Storegga tsunami sedimentation patterns with modelled wave heights: A discussion from the Shetland Isles field laboratory, Sedimentology, 67, 1344–1353, https://doi.org/10.1111/sed.12643, 2020.

de' Michieli Vitturi, M., Esposti Ongaro, T., Lari, G., and Aravena, A.: IMEX_SfloW2D 1.0: a depth-averaged numerical flow model for pyroclastic avalanches, Geoscientific Model Development, 12, 581–595, https://doi.org/10.5194/gmd-12-581-2019, 2019.

de' Michieli Vitturi, M., Esposti Ongaro, T., and Engwell, S.: IMEX_SfloW2D v2: a depth-averaged numerical flow model for volcanic gas–particle flows over complex topographies and water, Geoscientific Model Development, 16, 6309–6336, https://doi.org/10.5194/gmd-16-6309-2023, 2023.

Escalante, C., Fernández-Nieto, E. D., Morales de Luna, T., and Castro, M. J.: An Efficient Two-Layer Non-hydrostatic Approach for Dispersive Water Waves, J. Sci. Comput., 79, 273–320, https://doi.org/10.1007/s10915-018-0849-9, 2019.

Esposti Ongaro, T., de' Michieli Vitturi, M., Cerminara, M., Fornaciai, A., Nannipieri, L., Favalli, M., Calusi, B., Macías, J., Castro, M. J., Ortega, S., González-Vida, J. M., and Escalante, C.: Modeling tsunamis generated by submarine landslides at Stromboli volcano (Aeolian Islands, Italy): A numerical benchmark study, Front. Earth Sci., 9, 1–21, https://doi.org/10.3389/feart.2021.628652, 2021.

Esposti Ongaro, T., Cerminara, M., de' Michieli Vitturi, M., Tadini, A., Trolese, M., Fornaciai, A., Nannipieri, L., Calusi, B., Macías, J., Castro, M. J., Escalante, C., Ortega, S., González-Vida, J. M., and Rodríguez-Gálvez, J. F.: Modeling and numerical simulation of volcanic mass movements and associated tsunamis at Stromboli (Aeolian archipelago, Tyrrhenian sea, Italy), Front. Earth Sci., 2025.

Favalli, M., Fornaciai, A., and Pareschi, M. T.: LIDAR strip adjustment: Application to volcanic areas, Geomorphology, 111(3-4), 123–135, https://doi.org/10.1016/j.geomorph.2009.04.010, 2009.

Fernández-Nieto, E. D., Bouchut, F., Bresch, D., Castro Díaz, M. J., and Mangeney, A.: A new Savage–Hutter type model for submarine avalanches and generated tsunami, J. Comput. Phys., 227, 7720–7754, https://doi.org/10.1016/j.jcp.2008.04.039, 2008.

Fernández-Nieto, E. D., Parisot, M., Penel, Y., and Sainte-Marie, J.: A hierarchy of dispersive layer-averaged approximations of Euler equations for free surface flows, Comm. Math. Sci., 16, 1169–1202, https://doi.org/10.4310/CMS.2018.v16.n5.a1, 2018.

Fine, I. V., Rabinovich, A. B., Thomson, R. E., and Kulikov, E. A.: Numerical Modeling of Tsunami Generation by Submarine and Subaerial Landslides, in: Submarine Landslides and Tsunamis, edited by Yalçiner, A. C., Pelinovsky, E. N., Okal, E., and Synolakis, C. E., vol. 21 of *NATO Science Series*, Springer, Dordrecht, https://doi.org/10.1007/978-94-010-0205-9_9, 2003.

Fornaciai, A., Favalli, M., and Nannipieri, L.: Numerical simulation of the tsunamis generated by the Sciara del Fuoco landslides (Stromboli Island, Italy), Sci. Rep., 9, 18 542, https://doi.org/10.1038/s41598-019-54949-7, 2019.

Fornaciai, A., Favalli, M., and Nannipieri, L.: Reconstruction of the 2002 tsunami at Stromboli using the non-hydrostatic WAVE model (NHWAVE), in: Volcanic Island: from Hazard Assessment to Risk Mitigation, edited by Marotta, E., D'Auria, L., Zaniboni, F., and Nave, R., Geological Society Special Publication, https://doi.org/10.1144/SP519, 2024.

Fritz, H. M., Hager, W. H., and Minor, H. E.: Near field characteristics of landslide generated impulse waves, Journal of Waterway, Port, Coastal, and Ocean Engineering, 130, 287–302, https://doi.org/10.1061/(ASCE)0733-950X(2004)130:6(287), 2004.

Gatel, L., Lauvernet, C., Carluer, N., Weill, S., Tournebize, J., and Paniconi, C.: Global evaluation and sensitivity analysis of a physically based flow and reactive transport model on a laboratory experiment, Environmental Modelling & Software, 113, 73–83, https://doi.org/10.1016/j.envsoft.2018.12.006, 2019.

Giordano, G. and De Astis, G.: The summer 2019 basaltic Vulcanian eruptions (paroxysms) of Stromboli, Bull. Volcanol., 83, 1, https://doi.org/10.1007/s00445-020-01423-2, 2020.

González-Vida, J. M., Macías, J., Castro, M. J., Sánchez-Linares, C., de la Asunción, M., Ortega-Acosta, S., and Arcas, D.: The Lituya Bay landslide-generated mega-tsunami – numerical simulation and sensitivity analysis, Natural Hazards and Earth System Sciences, 19, 369–388, https://doi.org/10.5194/nhess-19-369-2019, 2019.

Grilli, S. T., Shelby, M., Kimmoun, O., Dupont, G., Nicolsky, D., Ma, G., Kirby, J. T., and Shi, F.: Modeling coastal tsunami hazard from submarine mass failures: effect of slide rheology, experimental validation, and case studies off the US East Coast, Nat. Hazards, 86, 353–391, https://doi.org/10.1007/s11069-016-2692-3, 2017.

Grilli, S. T., Tappin, D. R., Carey, S., Watt, S. F., Ward, S. N., Grilli, A. R., Engwell, S. L., Zhang, C., Kirby, J. T., Schambach, L., and Muin, M.: Modelling of the tsunami from the December 22, 2018 lateral collapse of Anak Krakatau volcano in the Sunda Straits, Indonesia, Sci. Rep., 9, 11 946–11 946, https://doi.org/10.1038/s41598-019-48327-6, 2019.

Harbitz, C. B., Løvholt, F., Pedersen, G., and Masson, D. G.: Mechanisms of tsunami generation by submarine landslides: a short review, Norweg. J. Geol., 86, 255–264, 2006.

Heidarzadeh, M., Ishibe, T., Sandanbata, O., Muhari, A., and Wijanarto, A.: Numerical modelling of the subaerial landslide source of the 22 December 2018 Anak Krakatoa volcanic tsunami, Ocean Engineering, https://doi.org/10.1016/j.oceaneng.2019.106733, 2020.

Heller, V., Bruggemann, M., Spinneken, J., and Rogers, B. D.: Composite modelling of subaerial landslide–tsunamis in different water body geometries and novel insight into slide and wave kinematics, Coastal Engineering, 109, 20–41, https://doi.org/10.1016/j.coastaleng.2015.12.004, 2016.

Homma, T. and Saltelli, A.: Importance measures in global sensitivity analysis of nonlinear models, Reliability Engineering & System Safety, 52, 1–17, https://doi.org/10.1016/0951-8320(96)00002-6, 1996.

Huang, B., Zhang, Q., Wang, J., Luo, C., Chen, X., and Chen, L.: Experimental study on impulse waves generated by gravitational collapse of rectangular granular piles, Physics of Fluids, 32, 033 301, https://doi.org/10.1063/1.5138709, 2020.

Ioki, K., Tanioka, Y., Yanagisawa, H., and Kawakami, G.: Numerical simulation of the landslide and tsunami due to the 1741 Oshima-Oshima eruption in Hokkaido, Japan, J. Geophys. Res., 124, 1991–2002, https://doi.org/10.1029/2018JB016166, 2019.

Kelfoun, K., Samaniego, P., Palacios, P., and Barba, D.: Testing the suitability of frictional behaviour for pyroclastic flow simulation by comparison with a well-constrained eruption at Tungurahua volcano (Ecuador), Bulletin of Volcanology, 71, 1057–1075, 2009.

Kelfoun, K., Gueugneau, V., Komorowski, J.-C., Aisyah, N., Cholik, N., and Merciecca, C.: Simulation of block-and-ash flows and ash-cloud surges of the 2010 eruption of Merapi volcano with a two-layer model, Journal of Geophysical Research: Solid Earth, 122, 4277–4292, https://doi.org/10.1002/2017JB013981, 2017.

Kirby, J., Grilli, S., Horrillo, J., Liu, P., Nicolsky, D., Abadie, S., Ataie-Ashtiani, B., Castro, M., Clous, L., Escalante Sánchez, C., Fine, I., González-Vida, J., Løvholt, F., Lynett, P., Ma, G., Macías, J., Ortega, S., Shi, F., Yavari, S., and Zhang, C.: Validation and inter-comparison of models for landslide tsunami generation, Ocean Model., 170, 101 943, https://doi.org/10.1016/j.ocemod.2021.101943, 2022.

Kubota, T., Saito, T., and Nishida, K.: Global fast-traveling tsunamis driven by atmospheric Lamb waves on the 2022 Tonga eruption, Science, 377, 91–94, https://doi.org/10.1126/science.abo4364, 2022.

Lacanna, G. and Ripepe, M.: Genesis of tsunami waves generated by pyroclastic flows and the early-warning system, in: Rittmann Conference 2020, Session S13. The Summer 2019 Stromboli Paroxysms: A Precious Opportunity to Expand the Knowledge on the Volcano, Catania, 2020.

Lucas, A., Mangeney, A., and Ampuero, J.-P.: Frictional velocity-weakening in landslides on Earth and on other planetary bodies, Nature Communications, 5, 3417, https://doi.org/10.1038/ncomms4417, 2014.

Løvholt, F., Harbitz, C. B., and Haugen, K. B.: A parametric study of tsunamis generated by submarine slides in the Ormen Lange/Storegga area off western Norway, Marine Petrol. Geol., 22, 219–231, https://doi.org/10.1016/j.marpetgeo.2004.10.017, 2005.

Løvholt, F., Pedersen, G., Harbitz, C. B., Glimsdal, S., and Kim, J.: On the characteristics of landslide tsunamis, Philos. T. R. Soc. A, 373, https://doi.org/10.1098/rsta.2014.0376, 2015.

Løvholt, F., Glimsdal, S., and Harbitz, C. B.: On the landslide tsunami uncertainty and hazard, Landslides, 17, 2301–2315, https://doi.org/10.1007/s10346-020-01429-z, 2020.

Macías, J., Vázquez, J. T., Fernández-Salas, L. M., González-Vida, J. M., Bárcenas, P., Castro, M. J., Díaz-del Río, V., and Alonso, B.: The Al-Borani submarine landslide and associated tsunami: A modelling approach, Marine Geology, 361, 79–95, https://doi.org/10.1016/j.margeo.2014.12.006, 2015.

Macías, J., Castro, M. J., Ortega, S., and González-Vida, J. M.: Performance assessment of Tsunami-HySEA model for NTHMP tsunami currents benchmarking. Field cases, Ocean Model., 152, 101 645, https://doi.org/10.1016/j.ocemod.2020.101645, 2020.

Macías, J., Escalante, C., and Castro, M. J.: Multilayer-HySEA model validation for landslide-generated tsunamis – Part 1: Rigid slides, Nat. Hazards Earth Syst. Sci., 21, 775–789, https://doi.org/10.5194/nhess-21-775-2021, 2021a.

Macías, J., Escalante, C., and Castro, M. J.: Multilayer-HySEA model validation for landslide-generated tsunamis – Part 2: Granular slides, Nat. Hazards Earth Syst. Sci., 21, 791–805, https://doi.org/10.5194/nhess-21-791-2021, 2021b.

Mangeney, A., Bouchut, F., Thomas, N., Vilotte, J., and Bristeau, M.: Numerical modeling of self-channeling granular flows and of their levee-channel deposits, J. Geophys. Res. Earth Surf., 112, F02 017, https://doi.org/10.1029/2006JF000469, 2007.

McMurtry, G. M., Watts, P., Fryer, G. J., Smith, J. R., and Imamura, F.: Giant landslides, mega-tsunamis and paleo-sea level in the Hawaiian Islands, Mar. Geol., 203, 219–233, https://doi.org/10.1016/S0025-3227(03)00306-2, 2004.

Moore, J. G. and Moore, G. W.: Deposit from a giant wave on the island of Lanai, Hawaii, Science, 226, 1312–1315, https://doi.org/10.1126/science.226.4680.131, 1984.

Nguyen, N. H. T.: Collapse of partially and fully submerged granular column generating impulse waves: An empirical law of maximum wave amplitude based on coupled multiphase fluid–particle modeling results, Physics of Fluids, 34, 013 310, https://doi.org/10.1063/5.0076755, 2022.

Omira, R., Ramalho, R. S., Kim, J., González, P. J., Kadri, U., Miranda, J. M., Carrilho, F., and Baptista, M. A.: Global Tonga tsunami explained by a fast-moving atmospheric source, Nature, 609, 734–740, https://doi.org/10.1038/s41586-022-04926-4, 2022.

Paris, R.: Source mechanisms of volcanic tsunamis, Philos. Trans. R. Soc. A, 373, 20140 380, https://doi.org/10.1098/rsta.2014.0380, 2015.

Paris, R., Switzer, A. D., Belousova, M., Belousov, A., Ontowirjo, B., Whelley, P. L., and Ulvrova, M.: Volcanic tsunami: A review of source mechanisms, past events and hazards in Southeast Asia (Indonesia, Philippines, Papua New Guinea), Nat. Hazards, 70, 447–470, https://doi.org/10.1007/s11069-013-0822-8, 2014.

Paris, R., Bravo, J. J. C., Gonzàlez, M. E. M., Kelfoun, K., and Nauret, F.: Explosive eruption, flank collapse and mega-tsunami at Tenerife ca. 170 ka, Nat. Commun., 8, 15 246, https://doi.org/10.1038/ncomms15246, 2017.

Pedrosa-González, M. T., González-Vida, J. M., Galindo-Záldivar, J., Ortega, S., Castro, M. J., Casas, D., and Ercilla, G.: Simulation of tsunami induced by a submarine landslide in a glaciomarine margin: the case of Storfjorden LS-1 (southwestern Svalbard Islands), Natural Hazards and Earth System Sciences, 22, 3839–3858, https://doi.org/10.5194/nhess-22-3839-2022, 2022.

Pelanti, M., Bouchut, F., and Mangeney, A.: A Roe-Type Scheme for Two-Phase Shallow Granular Flows with Bottom Topography, ESAIM: Mathematical Modelling and Numerical Analysis, 48, 851–885, https://doi.org/10.1051/m2an:2008029, 2008.

Peregrine, D. H.: Equations for water waves and the approximations behind them, Waves on beaches and resulting sediment transport, pp. 95–121, 1972.

Pistolesi, M., Bertagnini, A., di Roberto, A., Ripepe, M., and Rosi, M.: Tsunami and tephra deposits record interactions between past eruptive activity and landslides at Stromboli volcano, Italy, Geology, pp. 1–5, https://doi.org/10.1130/G47331.1, 2020.

Pitman, E. B. and Le, I.: A two-fluid model for avalanche and debris flows, Philosophical Transactions of the Royal Society A: Mathematical, Physical and Engineering Sciences, 363, 1573–1601, 2005.

Poulain, P., Le Friant, A., Pedreros, R., Mangeney, A., Filippini, A. G., Grandjean, G., Lemoine, A., Fernández-Nieto, E. D., Castro Díaz, M. J., and Peruzzetto, M.: Numerical simulation of submarine landslides and generated tsunamis: application to the on-going Mayotte seismo-volcanic crisis, Comptes Rendus. Géoscience, 354, 361–390, https://doi.org/10.5802/crgeos.138, 2022.

Poulain, P., Le Friant, A., Mangeney, A., Viroulet, S., Fernandez-Nieto, E., Castro Diaz, M., Peruzzetto, M., Grandjean, G., Bouchut, F., Pedreros, R., and Komorowski, J.-C.: Performance and limits of a shallow-water model for landslide-generated tsunamis: from laboratory experiments to simulations of flank collapses at Montagne Pelée (Martinique), Geophysical Journal International, 233, 796–825, https://doi.org/10.1093/gji/ggac482, 2023.

Pouliquen, O. and Forterre, Y.: Friction law for dense granular flows: application to the motion of a mass down a rough inclined plane, J. Fluid Mech., 453, 133–151, https://doi.org/10.1017/S0022112001006796, 2002.

Pudasaini, S. P. and Mergili, M.: A multi-phase mass flow model, Journal of Geophysical Research: Earth Surface, 124, 2920–2942, https://doi.org/10.1029/2019JF005204, 2019.

Ramalho, R. S., Winckler, G., Madeira, J., Helffrich, G. R., Hipólito, A., Quartau, R., Adena, K., and Schaefer, J. M.: Hazard potential of volcanic flank collapses raised by new megatsunami evidence, Sci. Adv., 1, e1500 456, https://doi.org/10.1126/sciadv.1500456, 2015.

Ripepe, M. and Lacanna, G.: Volcano generated tsunami recorded in the near source, Nat. Commun., 15, 1802, https://doi.org/10.1038/s41467-024-45937-1, 2024.

Robbe-Saule, M., Morize, C., Bertho, Y., Sauret, A., Hildenbrand, A., and Gondret, P.: From laboratory experiments to geophysical tsunamis generated by subaerial landslides, Scientific Reports, 11, 18 437, https://doi.org/10.1038/s41598-021-96369-6, 2021a.

Robbe-Saule, M., Morize, C., Henaff, R., Bertho, Y., Sauret, A., and Gondret, P.: Experimental investigation of tsunami waves generated by granular collapse into water, Journal of Fluid Mechanics, 907, A11, https://doi.org/10.1017/jfm.2020.807, 2021b.

Rosi, M., Bertagnini, A., and Landi, P.: Onset of the persistent activity at Stromboli Volcano (Italy), Bull. Volcanol., 62, 294–300, https://doi.org/10.1007/s004450000098, 2000.

Rosi, M., Pistolesi, M., Bertagnini, A., Landi, P., Pompilio, M., and Di Roberto, A.: Stromboli Volcano, Aeolian Islands (Italy): present eruptive activity and hazards, in: The Aeolian Islands Volcanoes, edited by Lucchi, F., Peccerillo, A., Keller, J., Tranne, C. A., and Rossi, P. L., vol. 37, Geological Society of London, https://doi.org/10.1144/M37.14, 2013.

Rosi, M., Levi, S. T., Pistolesi, M., Bertagnini, A., Brunelli, D., Cannavò, V., Di Renzoni, A., Ferranti, F., Renzulli, A., and Yoon, D.: Geoarchaeological evidence of middle-age tsunamis at Stromboli and consequences for the tsunami hazard in the Southern Tyrrhenian Sea, Scientific Reports, 9, 1–10, https://doi.org/10.1038/s41598-018-37050-3, 2019.

Sarri, A., Guillas, S., and Dias, F.: Statistical emulation of a tsunami model for sensitivity analysis and uncertainty quantification, Nat. Hazards Earth Syst. Sci., 12, 2003–2018, https://doi.org/10.5194/nhess-12-2003-2012, 2012.

Schindelé, F., Kong, L., Lane, E. M., Paris, R., Ripepe, M., Titov, V., and Bailey, R.: A Review of Tsunamis Generated by Volcanoes (TGV) Source Mechanism, Modelling, Monitoring and Warning Systems, Pure and Applied Geophysics, 181, 1745–1792, https://doi.org/10.1007/s00024-024-03515-y, 2024.

Shimizu, H., Koyaguchi, T., and Suzuki, Y.: A numerical shallow-water model for gravity currents for a wide range of density differences, Progress in Earth and Planetary Science, 4, 8, https://doi.org/10.1186/s40645-017-0120-2, 2017.

Snelling, B., Neethling, S., Horsburgh, K., Collins, G., and Piggott, M.: Uncertainty quantification of landslide generated waves using Gaussian process emulation and variance-based sensitivity analysis, Water, 12, 416, https://doi.org/10.3390/w12020416, 2020.

Sobol, I. M.: Sensitivity analysis for non-linear mathematical models (translated from Russian), Mathematical Modelling and Computational Experiment, 1, 407–414, 1993.

Sobol, I. M.: Global sensitivity indices for nonlinear mathematical models and their Monte Carlo estimates, Mathematics and Computers in Simulation, 55, 271–280, https://doi.org/10.1016/S0378-4754(00)00270-6, 2001.

Svennevig, K., Hicks, S. P., Forbriger, T., Lecocq, T., Widmer-Schnidrig, R., Mangeney, A., Hibert, C., Korsgaard, N. J., Lucas, A., Satriano, C., Anthony, R. E., Mordret, A., Schippkus, S., Rysgaard, S., Boone, W., Gibbons, S. J., Cook, K. L., Glimsdal, S., Løvholt, F., van Noten, K., Assink, J. D., Marboeuf, A., Lomax, A., Vanneste, K., Taira, T., Spagnolo, M., De Plaen, R., Koelemeijer, P., Ebeling, C., Cannata, A., Harcourt, W. D., Cornwell, D. G., Caudron, C., Poli, P., Bernard, P., Larose, E., Stutzmann, E., Voss, P. H., Lund, B., Cannavo, F., Castro-Díaz, M. J., Chaves, E., Dahl-Jensen, T., de Pinho Dias, N., Déprez, A., Develter, R., Dreger, D., Evers, L. G., Fernández-Nieto, E. D., Ferreira, A. M. G., Funning, G., Gabriel, A.-A., Hendrickx, M., Kafka, A. L., Keiding, M., Kerby, J., Khan, S. A., Kjær Dideriksen, A., Lamb, O. D., Larsen, T. B., Lipovsky, B., Magdalena, I., Malet, J.-P., Myrup, M., Rivera, L., Ruiz-Castillo, E., Wetter, S., and Wirtz, B.: A rockslide-generated tsunami in a Greenland fjord rang Earth for 9 days, Science, 385, 1196–1205, https://doi.org/10.1126/science.adm9247, 2024.

Tadini, A., Bevilacqua, A., de' Michieli Vitturi, M., Bonilauri, E., Harris, A., Cerminara, M., Esposti Ongaro, T., Neri, A., Paris, R., Pistolesi, M., Trolese, M., Rodriguez Gàlvez, J. F., Andronico, D., Bertagnini, A., Calvari, S., Casalbore, D., Cassidy, M., Civico, R., Del Bello, E., Di Roberto, A., Di Traglia, F., Fornaciai, A., Grezio, A., Gurioli, L., Harbitz, C. B., Lacanna, G., Løvholt, F., Marani, M., Pompilio, M., Ricci, T., Rosi, M., Sandri, L., Esclasans, R. U., and Voloschina, M.: Probabilistic tsunami hazard assessment at Stromboli volcano: 1. Review of historical sources and expert elicitation findings, Natural Hazards and Earth System Sciences, in preparation.

Tinti, S., Pagnoni, G., and Zaniboni, F.: The landslides and tsunamis of the 30th of December 2002 in Stromboli analysed through numerical simulations, Bulletin of Volcanology, 68, 462–479, https://doi.org/10.1007/s00445-005-0022-9, 2006.

Tinti, S., Zaniboni, F., Pagnoni, G., and Manucci, A.: Stromboli island (Italy): Scenarios of tsunamis generated by submarine landslides, Pure Appl. Geophys., 165, 2143–2167, https://doi.org/10.1007/978-3-0346-0057-6_9, 2008.

Urgeles, R., Bahk, J. J., Lee, S. H., Horozal, S., Cukur, D., Kim, S. P., and Um, I. K.: Tsunami hazard from submarine landslides: scenario-based assessment in the Ulleung Basin, East Sea (Japan Sea), Geosciences Journal, 23, 439–460, https://doi.org/10.1007/s12303-018-0044-x, 2019.

Vicari, H. and Issler, D.: MoT-PSA: a two-layer depth-averaged model for simulation of powder snow avalanches on 3-D terrain, Annals of Glaciology, 65, e16, https://doi.org/10.1017/aog.2024.10, 2025.

Virtanen, P., Gommers, R., Oliphant, T. E., et al.: SciPy 1.0: Fundamental Algorithms for Scientific Computing in Python, Nature Methods, 17, 261–272, https://doi.org/10.1038/s41592-019-0686-2, 2020.

Ward, S. N. and Day, S.: Ritter Island Volcano—lateral collapse and the tsunami of 1888, Geophysical Journal International, 154, 891–902, https://doi.org/10.1046/j.1365-246X.2003.02016.x, 2003.

Wünnemann, K. and Weiss, R.: The meteorite impact-induced tsunami hazard, Philosophical Transactions of the Royal Society A: Mathematical, Physical and Engineering Sciences, 373, 20140 381, https://doi.org/10.1098/rsta.2014.0381, 2015.

Yavari-Ramshe, S. and Ataie-Ashtiani, B.: Numerical modeling of subaerial and submarine landslide-generated tsunami waves—recent advances and future challenges, Landslides, 13, 1325–1368, https://doi.org/10.1007/s10346-016-0734-2, 2016.

Yavari-Ramshe, S. and Ataie-Ashtiani, B.: On the effects of landslide deformability and initial submergence on landslide-generated waves, Landslides, 16, 37–53, https://doi.org/10.1007/s10346-018-1061-6, 2019.

Ye, L., Kanamori, H., Rivera, L., Lay, T., Zhou, Y., Sianipar, D., and Satake, K.: The 22 December 2018 tsunami from flank collapse of Anak Krakatau volcano during eruption, Sci. Adv., 6, eaaz1377, https://doi.org/10.1126/sciadv.aaz1377, 2020.

Zhao, H., Amann, F., and Kowalski, J.: Emulator-based global sensitivity analysis for flow-like landslide run-out models, Landslides, 18, 3299–3314, https://doi.org/10.1007/s10346-021-01690-w, 2021.